Research Square

Preprints are preliminary reports that have not undergone peer review.
They should not be considered conclusive, used to inform clinical practice,
or referenced by the media as validated information.

Computational modeling of the fast-to-slow EEG rhythm transition across seizure evolution and postictal recovery

Feng Zhang
Tianjin University
Meili Lu
Tianjin University of Technology and Education
Xile Wei
xileweі@tju.edu.cn

Tianjin University

Research Article

Keywords:

Posted Date: November 13th, 2026

DOI: https://doi.org/10.21203/rs.3.rs-11531913/v1

License: This work is licensed under a Creative Commons Attribution 4.0 International License.
Read Full License

Additional Declarations: No competing interests reported.

Computational modeling of the fast-to-slow EEG rhythm transition across seizure evolution and postictal recovery

Feng Zhang[1], Meili Lu[2], Xile Wei[1*]

[1]Tianjin Key Laboratory of Process Measurement and Control, School of Electrical and Information Engineering, Tianjin University, Tianjin, 300072, China.
[2]School of Information Technology Engineering, Tianjin University of Technology and Education, Tianjin, 300222, China.

*Corresponding author(s). E-mail(s): xilewei@tju.edu.cn;

Abstract

Epileptic electroencephalography (EEG) can exhibit progressive rhythm slowing across seizure evolution and postictal recovery. How fast ictal activity and slower recovery-related processes generate this fast-to-slow rhythm transition within recurrent seizure cycles remains poorly understood. This study aimed to reproduce and explain this spectral evolution using a dynamical model. To provide an empirical reference, we characterized spectral evolution in 33 seizures from 11 patients using time-frequency analysis. Within-patient analysis showed ictal slowing followed by retained relative low-frequency weighting during early postictal recovery, whereas postictal trajectories varied across patients. We developed a Dual-Component Epileptic EEG (DCE) model comprising two coupled subsystems: one generates fast ictal discharges and spontaneous interictal–ictal transitions; the other governs transitions among fast spikes, spike–wave discharges, and slow waves. The model qualitatively reproduced the fast-to-slow rhythm transition and delineated interictal, ictal, and postictal phases. Three parameter families regulated distinct transition features: timescale ratios set spectral span, filtering rates governed temporal organization, and connectivity coefficients shaped oscillatory-regime composition by shifting bifurcation thresholds. In simulations of two coupled DCE nodes, coupling strength controlled the extent of recruited rhythm slowing, and recruited events exhibited longer model-defined postictal durations than spontaneous events. By linking recurrent interictal–ictal switching with spectral evolution, the DCE model provides a unified dynamical account of fast-to-slow rhythm transitions and their variability. Its model-defined ictal–postictal boundary may support patient-specific estimation of electrographic seizure offset. Inter-node differences in rhythm slowing and postictal duration may serve as candidate dynamical signatures for distinguishing driving from recruited nodes in epileptic networks.

Keywords: epilepsy, electroencephalography (EEG), spectral evolution, seizure dynamics, postictal recovery, spike–wave discharge

1 Introduction

Epilepsy is a chronic neurological disorder characterized by spontaneous and recurrent seizures, which arise from abnormal neuronal discharges in the brain. Electroencephalography (EEG) provides a macroscopic window into the collective rhythmic activity of neuronal populations, playing an essential role in seizure detection, presurgical

evaluation, and epileptic network analysis (Wong et al. 2023; Rosenow and Lüders 2001; Bartolomei et al. 2008). Clinical and electrophysiological studies use specific EEG markers to characterize epileptiform activity and, particularly in focal epilepsy, support delineation of the epileptogenic zone. These markers span diverse timescales: low-voltage fast activity (LVFA) and high-frequency oscillations (HFOs) represent fast epileptiform activity (Perucca et al. 2014; Frauscher et al. 2017; Zijlmans et al. 2012); interictal epileptiform discharges (IEDs), such as spikes and sharp waves, capture abnormal paroxysmal events (De Curtis et al. 2001; Kane et al. 2017); and spike–wave discharges (SWDs), slow waves, and direct-current shifts involve slower rhythmic activity or sustained potential shifts (Sitnikova 2010; Sheybani et al. 2025; Lee et al. 2020). These structured discharge patterns in epileptic EEG are not merely isolated signal abnormalities but reflect specific pathophysiological interactions among neuronal populations whose relative contributions change as a seizure progresses (Destexhe 1998). Therefore, epileptic EEG can be regarded as a temporally organized, multi-timescale process rather than a collection of independent electrographic events. This multi-timescale organization gives rise to rich spectral dynamics that may provide insights into mechanisms underlying seizure initiation, propagation, termination, and recovery (Jirsa et al. 2014; Wendling et al. 2016).

These spectral dynamics are particularly evident as EEG rhythms evolve across the ictal and postictal periods. During the ictal period, seizures often initiate with LVFA or fast tonic discharges in the gamma band and then evolve into slower clonic activity in the theta band (Perucca et al. 2014; Demont-Guignard et al. 2009; Wendling et al. 2003). After seizure termination, EEG activity does not immediately return to the interictal baseline; instead, the postictal state is commonly characterized by suppression or slowing of EEG rhythms, with delta slowing representing the most prominent postictal EEG change (So and Blume 2010; Pottkamper et al. 2020). These clinical observations indicate that the dominant rhythms of epileptic EEG tend to shift toward lower-frequency bands over the course of seizure evolution and postictal recovery. Quantitative analyses further support this view. Ictal propagation is accompanied by organized time–frequency structures (Hu et al. 2026), and seizure termination involves systematic spectral reorganization, including decreased spectral entropy and increased delta activity (Sanz-García et al. 2017). These findings suggest that postictal slowing should not be viewed as spectrally isolated from the preceding seizure, but may instead represent the slow terminal segment of a continuous downward spectral trajectory that begins during seizure evolution and extends into postictal recovery. In this study, we refer to this continuous downward ictal-to-postictal spectral trajectory as the *fast-to-slow rhythm transition*.

This spectral trajectory may reflect specific neural processes engaged at different stages of a seizure: fast activity at seizure onset, progressive rhythm slowing during seizure evolution, and subsequent slow-wave recovery have been associated with local activation of epileptic networks, large-scale synchronization, and postictal network reorganization, respectively (Bartolomei et al. 2008; Wendling et al. 2003; Tomlinson et al. 2018). Characterizing this spectral trajectory may therefore provide insights into the mechanisms underlying seizure dynamics. Clinical and experimental studies primarily establish associations between spectral EEG features and brain regions or clinical states. On their own, they do not provide a unified dynamical account of how this trajectory is generated or how fast- and slow-timescale processes interact during its evolution. Computational models can complement these studies by representing latent neural processes with a small number of state variables and parameters, thereby linking macroscopic EEG phenotypes to candidate neuronal and biophysical mechanisms (Wendling et al. 2016; Saggio et al. 2020).

Many mechanistic models of epileptic EEG are based on neural mass models (NMMs) (Wilson and Cowan 1972), which have reproduced specific epileptiform discharges observed in clinical EEG, such as fast ictal activity in temporal lobe epilepsy and SWDs in absence epilepsy (Wendling et al. 2002; Goodfellow et al. 2011; Taylor and Baier 2011). In addition to particular waveform classes, NMM-based studies have also modeled waveform evolution and frequency trajectories, including the downward chirp of fast-onset activity in focal epilepsy (Nevado-Holgado et al. 2012; Kayabas et al. 2024). Moreover, the Epileptor provides a canonical low-dimensional description of

spontaneous seizure onset and offset through transitions between interictal and ictal states (Jirsa et al. 2014). However, how interactions between fast ictal activity and slower recovery-related processes generate a continuous ictal-to-postictal spectral trajectory within recurrent seizure cycles remains insufficiently understood. To address this gap, we propose a phenomenological dynamical model, named the Dual-Component Epileptic EEG (DCE) model, to capture this spectral evolution. The model comprises two coupled subsystems operating on different timescales: the first describes fast ictal activity and spontaneous interictal–ictal transitions, whereas the second describes transitions among fast spikes, SWDs, and slow waves. The second subsystem is motivated by observations that fast ictal discharges and spike–wave complexes can overlap and evolve continuously during seizures (Aung et al. 2026). Through nonlinear interactions between the two subsystems, the DCE model links progressive ictal rhythm slowing to postictal slow activity while preserving spontaneous interictal–ictal switching. The primary novelties and contributions of this work are as follows:

- We characterize the fast-to-slow rhythm transition and its variability in clinical EEG and show that the DCE model qualitatively reproduces its principal spectral features.
- Within the DCE framework, coupled dynamics generate recurrent interictal–ictal–postictal cycles in which the fast-to-slow rhythm transition unfolds across the ictal and postictal phases.
- We investigate the variability of the rhythm transition and establish a parameter-to-phenotype decomposition, showing that three functionally distinct parameter families control different aspects of the transition.
- We extend the analysis to two coupled DCE nodes and characterize recruitment-induced rhythm transitions, showing that coupling strength governs the extent of rhythm slowing in the recruited node and that recruited events exhibit longer postictal durations than events in the driving node.

The rest of this paper is organized as follows. In Section 2, we introduce the DCE model step by step. In Section 3, we present the clinical characterization, simulation results, and dynamical analyses. In Section 4, we discuss the implications and limitations of these findings and outline future extensions. In Section 5, we draw conclusions.

2 Models and methods

2.1 Model overview: dual-component epileptic EEG model

The DCE model is developed to reproduce the progressive slowing of EEG rhythms across seizure evolution and postictal recovery. To achieve this, the model design is motivated by two signal-level observations. First, fast ictal discharges arise and terminate spontaneously, reflecting the recurrent nature of epileptic seizures. Second, fast ictal discharges and spike–wave complexes frequently overlap and evolve continuously during seizures (Aung et al. 2026). Accordingly, as illustrated in Fig. 1(a), the DCE model comprises two subsystems that capture these two temporal components. Subsystem I (x_1, y_1, z_1) generates fast ictal activity and governs spontaneous interictal–ictal transitions, whereas Subsystem II (x_2, y_2, z_2) governs transitions among fast spikes, SWDs, and slow waves. The two subsystems are nonlinearly coupled to enable mutual modulation between fast and slow components, thereby allowing the model to generate diverse rhythmic patterns. In this sense, the DCE model is a phenomenological model designed to describe the spectral evolution of epileptic EEG rather than to simulate neuronal populations in biophysical detail.

2.2 Subsystem I: fast ictal discharges and interictal–ictal transitions

Subsystem I is designed to generate fast ictal discharges and spontaneous interictal–ictal transitions. A canonical phenomenological model of *square-wave bursting* provides a compact description of such alternations between quiescent and active regimes (Jirsa et al. 2014; Ermentrout and Terman 2010). Its explicit separation of fast and slow dynamics provides a tractable framework for analyzing these recurrent state transitions. Based

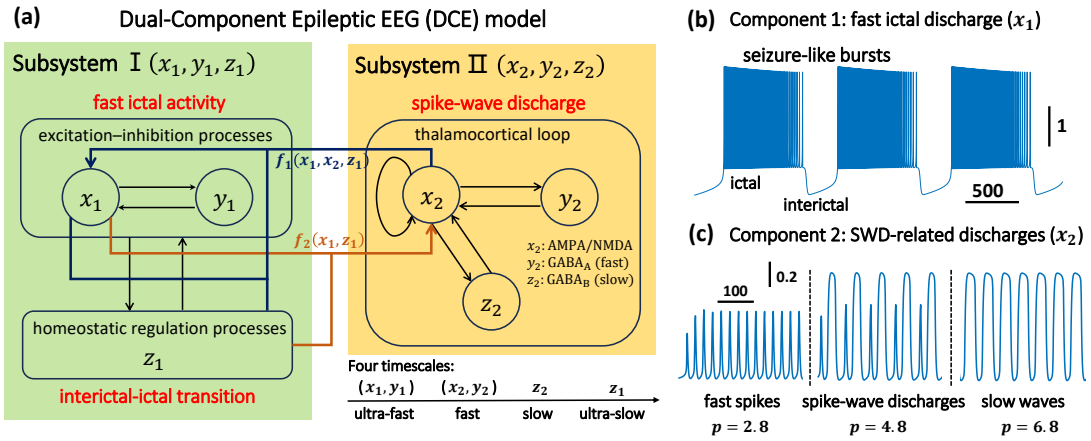


Fig. 1 Architecture and isolated-subsystem dynamics of the Dual-Component Epileptic EEG (DCE) model. **(a)** Schematic of the DCE model. Subsystem I generates fast ictal activity through x_1 and y_1 and recurrent interictal–ictal transitions through the ultraslow variable z_1. Subsystem II generates spike–wave discharge (SWD)-related dynamics through the fast variables x_2, y_2 and the slower variable z_2. The timescale ordering is shown below the schematic. The two subsystems interact through $f_1(x_1, x_2, z_1)$ (blue path) and $f_2(x_1, z_1)$ (orange path), defined in Section 2.4. Physiological annotations indicate possible qualitative interpretations of the model variables; see Sections 2.2 and 2.3 for details. **(b)** Time series of x_1 from isolated Subsystem I, showing recurrent seizure-like bursts. **(c)** Time series of x_2 from isolated Subsystem II at $p = 2.8$, 4.8, and 6.8, showing fast spikes, SWDs, and slow waves, respectively. Horizontal and vertical scale bars indicate model time and amplitude, respectively; both are dimensionless. AMPA, α-amino-3-hydroxy-5-methyl-4-isoxazolepropionic acid; NMDA, N-methyl-D-aspartate; GABA, γ-aminobutyric acid.

on this, Subsystem I is defined as follows:

$$\frac{dx_1}{dt} = \frac{-f_1(x_1) + y_1 - z_1 + x_0}{\tau_{x_1}}, \tag{1}$$

$$\frac{dy_1}{dt} = \frac{-y_1 - 5x_1^2 + y_0}{\tau_{y_1}}, \tag{2}$$

$$\frac{dz_1}{dt} = \frac{-z_1 + h(x_1; z_0)}{\tau_{z_1}}, \tag{3}$$

where

$$f_1(x_1) = x_1^3 - 3x_1^2, \tag{4}$$

$$h(x_1; z_0) = z_0 + 3/\left(1 + \exp\left(\frac{-x_1 - 0.5}{0.1}\right)\right), \tag{5}$$

with the timescales satisfying $\tau_{x_1} \approx \tau_{y_1} \ll \tau_{z_1}$. The fast variables x_1 and y_1 generate oscillatory activity in the (x_1, y_1) phase plane, corresponding to fast ictal discharges, whereas the slow variable z_1 shifts the x_1-nullcline ($\frac{dx_1}{dt} = 0$) and thereby controls transitions between active (ictal) and silent (interictal) phases. The parameters x_0 and y_0 act as constant bias terms in the subsystem. Importantly, the parameter z_0 controls the degree of epileptogenicity: for $z_0 < 2.95$, the subsystem generates spontaneous fast ictal discharges and is said to be epileptogenic; for $z_0 \geq 2.95$, it remains near equilibrium and is said to be non-epileptogenic. Unless stated otherwise, all parameters are taken from Table 1. Simulation results for Subsystem I at the default value $z_0 = 2.6$ are shown in Fig. 1(b), where the subsystem produces recurrent seizure-like bursts. This parameter-based definition of epileptogenicity is used in Section 3.4 when constructing driving and recruited nodes in the coupled analysis.

Although Subsystem I is phenomenological, its dynamics admit a qualitative physiological interpretation. The fast variables x_1 and y_1 capture rapid ictal activity, whereas z_1 provides ultraslow modulation of seizure recurrence. This timescale separation is motivated by the distinction between fast neuronal discharges and slower processes regulating network excitability (Jirsa et al. 2014). Extracellular ionic regulation, including glial potassium buffering, provides a possible physiological basis for such slow modulation (Frohlich et al. 2010).

2.3 Subsystem II: spike–wave discharge dynamics

Subsystem II generates spike–wave discharges and slow-wave activity through fast excitatory–inhibitory interactions coupled to slower inhibitory feedback. This effective fast–slow architecture is motivated by thalamocortical models

Table 1 Default parameter values for the DCE model.

Parameter	Value	Equation	Parameter	Value	Equation
τ_{x_1}	0.3	(1)	C_{xx}	23	(6)
τ_{y_1}	0.3	(2)	C_{yx}	-15	(6)
τ_{z_1}	1300	(3)	C_{zx}	-10	(6)
x_0	3.1	(1)	C_{xy}	35	(7)
y_0	1	(2)	C_{xz}	20	(8)
z_0	2.6	(3)	p	4.8[a]	(6)
τ_{x_2}	1	(6)	q	-4	(7)
τ_{y_2}	1	(7)	r	0	(8)
τ_{z_2}	80	(8)	γ_1, γ_2	0.001, 0.015	(10)

[a]The tabulated value of p applies only when Subsystem II is simulated in isolation. In the full DCE model, p is defined by the function $f_2(x_1, z_1)$ in Eq. (10).

of SWD generation (Destexhe 1998; Steriade and Contreras 1998). Following a reduced thalamocortical model based on the Wilson–Cowan formalism (Wang et al. 2012), Subsystem II is written as follows:

$$\frac{dx_2}{dt} = \frac{-x_2 + S(C_{xx}x_2 + C_{yx}y_2 + C_{zx}z_2 + p)}{\tau_{x_2}}, \tag{6}$$

$$\frac{dy_2}{dt} = \frac{-y_2 + S(C_{xy}x_2 + q)}{\tau_{y_2}}, \tag{7}$$

$$\frac{dz_2}{dt} = \frac{-z_2 + S(C_{xz}x_2 + r)}{\tau_{z_2}}, \tag{8}$$

where the timescales satisfy $\tau_{x_2} \approx \tau_{y_2} \ll \tau_{z_2}$, and $S(\cdot)$ denotes the sigmoidal activation function, $S(u) = 1/(1 + \exp[-(u - 4)])$. Here, x_2 and y_2 are interpreted as effective fast-timescale variables associated with excitatory and inhibitory population activity, respectively, whereas z_2 is interpreted as an effective slow-timescale variable associated with inhibitory feedback. The fast variables govern the rapid spike component of SWDs, whereas z_2 governs the subsequent slow-wave component. This separation between spike and wave timescales enables Subsystem II to generate SWD-like waveforms. The connectivity coefficients C_{ij} define interactions among these variables: $C_{xx} > 0$ controls self-excitation of x_2; $C_{xy} > 0$ and $C_{xz} > 0$ couple x_2 to y_2 and z_2; and $C_{yx} < 0$ and $C_{zx} < 0$ provide inhibitory feedback to x_2. The fast–slow feedback architecture has a qualitative analogue in thalamocortical models with fast excitation and inhibition and slower $GABA_B$-mediated feedback (Wang et al. 2012). The inputs p, q, and r set the excitability of the corresponding effective populations. Unless stated otherwise, all parameters are taken from Table 1. The input p is the main control parameter for Subsystem II. As shown in Fig. 1(c), varying p enables Subsystem II to generate distinct waveforms, including fast spikes, SWDs, and slow waves.

2.4 Nonlinear coupling between subsystems

The two subsystems are coupled bidirectionally so that the fast ictal component and the spike–wave and slow-rhythm components can modulate each other during the seizure-like bursts in Subsystem I.

Influence of Subsystem II on Subsystem I

To allow the firing activity generated by Subsystem II to shape the fast ictal discharges in Subsystem I, the function $f_1(x_1)$ in Eq. (1) is replaced by a state-dependent function:

$$f_1(x_1, x_2, z_1) = \begin{cases} x_1^3 - 3x_1^2, & x_1 < 0, \\ (2x_2 - 0.6(z_1 - 4)^2 - 1.3)x_1, & x_1 \geq 0. \end{cases} \tag{9}$$

At $x_1 = 0$, both branches of f_1 evaluate to zero, so the function is continuous across the switching boundary. However, its one-sided derivatives at $x_1 = 0$ are generally unequal: the left derivative is zero, whereas the right derivative is $2x_2 - 0.6(z_1 - 4)^2 - 1.3$. Thus, f_1 is continuous but only piecewise differentiable. Through this coupling, x_2 from Subsystem II modifies the positive

branch of the x_1-nullcline and thereby changes the amplitude envelope of fast ictal activity in Subsystem I. The z_1-dependent term acts as a slow phase-dependent gate, allowing the envelope modulation to vary across seizure evolution while constraining its amplitude to a bounded range.

Influence of Subsystem I on Subsystem II

Conversely, the SWD-generating subsystem is embedded into the interictal–ictal framework of Subsystem I. During the interictal period, Subsystem II should produce only isolated spikes rather than sustained oscillations. To embed the SWD dynamics into the interictal–ictal framework of Subsystem I, the external input p in Eq. (6) is redefined as a time-dependent drive:

$$p := f_2(x_1, z_1) = 3.39z_1 - 6.46 + \begin{cases} 2.5\gamma_1 \displaystyle\int_0^t e^{-\gamma_1(t-s)} x_1(s)\,\mathrm{d}s, & \dot{z}_1 \geq 0, \\ 2.5\gamma_2 \displaystyle\int_0^t e^{-\gamma_2(t-s)} x_1(s)\,\mathrm{d}s, & \dot{z}_1 < 0. \end{cases} \tag{10}$$

The linear term $3.39z_1 - 6.46$ in Eq. (10) links p to the slow variable z_1 of Subsystem I, while the convolution term implements low-pass filtering of the fast ictal activity x_1 in Subsystem I. The two filtering rates γ_1 and γ_2 are used during the rising and falling phases of z_1, respectively, allowing the filtered drive to Subsystem II to accumulate and decay with distinct temporal profiles. This asymmetry is systematically analyzed in Section 3.3.2.

After coupling the two subsystems, the simulated EEG of the whole DCE model is defined as $x_1 + 2x_2$. The six core state variables possess characteristic timescales that satisfy

$$\tau_{x_1} \approx \tau_{y_1} < \tau_{x_2} \approx \tau_{y_2} \ll \tau_{z_2} \ll \tau_{z_1}, \tag{11}$$

providing the multi-timescale structure required to generate ultrafast ictal discharges, fast spikes and slow waves in SWDs, and ultraslow modulation of the seizure phase within a unified framework.

2.5 Simulation methods

The DCE model is implemented in MATLAB R2022a. To account for background EEG fluctuations, zero-mean Gaussian white noise is added to the model equations. Specifically, mutually independent Wiener processes enter directly into Eqs. (1), (2), (6), (7), and (8), with diffusion intensities of 0.0001, 0.0001, 0.0015, 0.0015, and 0.00004, respectively. No stochastic input is applied to z_1. The numerical system is advanced jointly using a fixed integration step of $h = 0.025$. At each step, the deterministic drift is approximated using the classical fourth-order Runge–Kutta method, whereas the state-independent additive Wiener increment is incorporated once in Euler–Maruyama form. The complete stochastic formulation and numerical integration scheme are provided in Supplementary Section S1. A standalone MATLAB implementation of this numerical formulation is available at https://github.com/Fengzhang1998/Dual-Component-Epileptic-EEG-model.

It should be noted that the integration step $h = 0.025$ is defined in dimensionless model time, and one simulation sample is recorded at each integration step. For comparison with the clinical EEG analyzed in Section 3.1, whose sampling frequency is 512 Hz, the simulated output is assigned a sampling frequency of 512 Hz, such that 512 simulation samples correspond to 1 s. This fixed conversion is applied uniformly to all simulations when constructing the time and frequency axes for time–frequency analysis and when reporting simulated durations in seconds. It does not alter the model equations or numerical integration and should not be interpreted as a biophysical calibration of the model timescales.

3 Results

3.1 Characterization of the fast-to-slow rhythm transition in clinical EEG

Earlier studies have documented ictal rhythm slowing and postictal delta activity, motivating our definition of the fast-to-slow rhythm transition. Here, we characterized clinical EEG spectral evolution across the ictal and early postictal periods to examine the relationship between these phenomena. This analysis provided an empirical reference for the DCE model and assessed variability across seizures and patients.

The clinical EEG data analyzed here were obtained from the publicly available Siena Scalp

EEG dataset (Detti 2020), which contains 47 annotated seizures from 14 patients (Supplementary Table S1), recorded at 512 Hz using the international 10–20 electrode system. Most nominal acquisition passbands reported in the EDF metadata covered 2–30 Hz (Supplementary Table S2); we therefore adopted this frequency range for cross-patient spectral analysis. Recordings were included when their nominal high-pass cutoff was below 2 Hz and their low-pass cutoff was at or above 30 Hz, yielding 33 seizures from 11 patients. Patient PN00 was selected for detailed illustration because its recordings clearly displayed the spectral evolution motivating the computational model. Participant information and recording selection are detailed in Supplementary Section S2.1.

Although the postictal state may persist for minutes to hours (Pottkamper et al. 2020), our analysis focused on spectral evolution around the immediate ictal–postictal transition. For each seizure of duration D, the analysis window extended from the clinically annotated seizure onset to D seconds after the annotated seizure offset, thereby including the complete annotated ictal period and an equally long interval of early postictal recovery. We quantified spectral evolution using both short-time Fourier transform (STFT) and continuous wavelet transform (CWT). Three complementary spectral features were calculated from linear spectral power over 2–30 Hz. The spectral centroid (SC) is the power-weighted mean frequency, and the median frequency (MF) divides the analyzed spectral power into equal halves. The low-frequency ratio (LFR) is the proportion of 2–8 Hz power within the total 2–30 Hz power. It reflects the relative contribution of delta/theta activity within the analyzed portion of the delta-to-beta range. Transform parameters for STFT and CWT, spectral feature equations, and absolute-power calculations are detailed in Supplementary Section S2.2.

Fig. 2(a1,a2) shows simultaneous EEG recordings from T5 and O2 during the same seizure in Patient PN00. The matched enlarged views reveal more prominent rapid fluctuations in T5 than O2 (Fig. 2(a3,a4)). This waveform difference is consistent with the stronger broadband fast ictal activity in T5 shown by the STFT spectrograms (Fig. 2(b)). The CWT spectrograms revealed the lower-frequency evolution more clearly. During the later ictal interval, spectral power shifted toward lower frequencies, with low-frequency activity persisting beyond the annotated offset (Fig. 2(c)). This evolution was visible in both electrodes despite their different levels of fast ictal activity. Correspondingly, SC and MF decreased and LFR increased over the later ictal portion of the event (Fig. 2(d)). This example illustrates ictal slowing and its relationship to early postictal spectral activity under contrasting ictal waveform expression within the same seizure.

We next examined whether this pattern recurred across seizures in Patient PN00. Four of its five annotated seizures met the harmonized 2–30 Hz passband criterion. For each eligible seizure, channel-level descriptors were interpolated to a common event-relative axis and summarized across eligible EEG channels using the pointwise median, with onset at 0, offset at 1, and the end of the matched postictal interval at 2. Median-based aggregation reduces sensitivity to extreme channel-level values (Wilcox and Rousselet 2023) and has been used to summarize EEG spectral measures across channels (Comsa et al. 2019). For phase comparisons, the early ictal, late ictal, and early postictal windows were defined as normalized times 0.10–0.40, 0.70–1.00, and 1.00–1.30, respectively. Ictal slopes were calculated over 0–1, and full-window slopes over 0–2 (Supplementary Table S3). All four PN00 seizures had negative ictal slopes for SC and MF and positive ictal slopes for LFR (Fig. 3(a–c)). In each event, early postictal SC and MF remained lower, and LFR higher, than in the early ictal window (Supplementary Table S3). Postictal trajectories nevertheless varied, with a pronounced transient rebound in Seizure 2. Additionally, dominant-frequency trajectories supported ictal slowing and retained early postictal low-frequency activity, consistent with the SC, MF, and LFR results (Supplementary Section S2.4 and Fig. S1). Using STFT instead of CWT also yielded negative ictal SC slopes and lower early-postictal than early-ictal SC values in all four PN00 events, although the absolute SC values and detailed trajectories differed between methods (Supplementary Fig. S2).

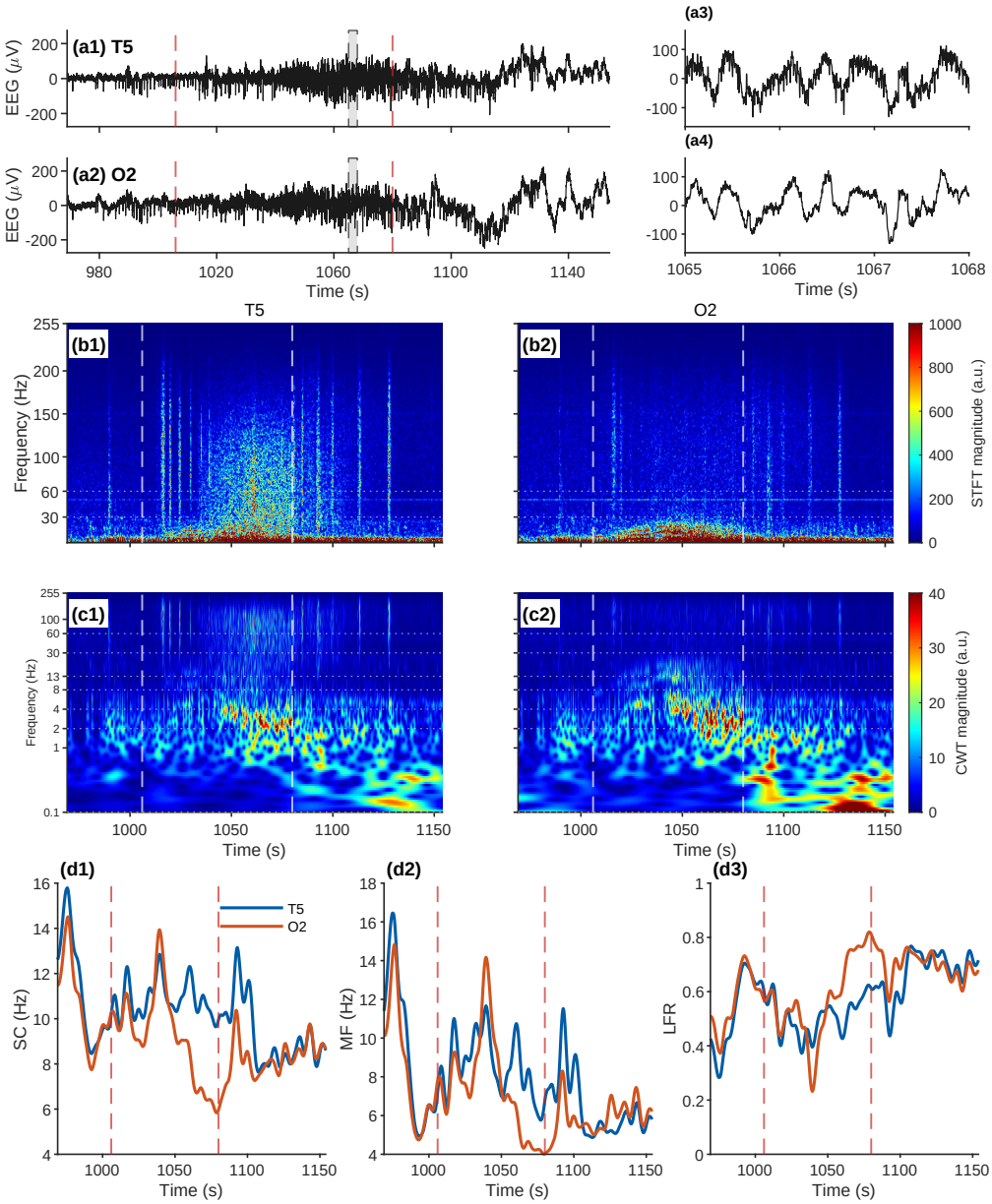


Fig. 2 Ictal-to-postictal spectral evolution in two EEG channels during one PN00 seizure. **(a)** Simultaneous EEG recordings from T5 (a1) and O2 (a2) during the fourth annotated seizure, with amplitudes in μV. Gray boxes mark the common late-ictal window (1065–1068 s) enlarged in (a3,a4), respectively. The two electrodes share identical axis limits within each column. **(b)** Short-time Fourier transform (STFT) spectrograms for T5 (b1) and O2 (b2), displayed over 0.1–255 Hz on linear frequency axes. **(c)** Continuous wavelet transform (CWT) spectrograms for the same electrodes (c1,c2), displayed over 0.1–255 Hz on logarithmic frequency axes. Color bars in (b,c) show transform magnitudes in arbitrary units (a.u.) on linear color scales; horizontal guides in (c) indicate frequency-band boundaries. **(d)** CWT-derived spectral centroid (SC, d1), median frequency (MF, d2), and low-frequency ratio (LFR, d3), calculated from linear power over 2–30 Hz. SC and MF are in Hz; LFR is the dimensionless fraction of 2–8 Hz power within 2–30 Hz. Blue and orange curves denote T5 and O2, respectively. All horizontal axes show seconds from the recording start. Dashed vertical lines mark the annotated onset and offset: red in (a1,a2,d), white in (b,c). Preictal activity and the wider display band provide context for the 2–30 Hz analysis.

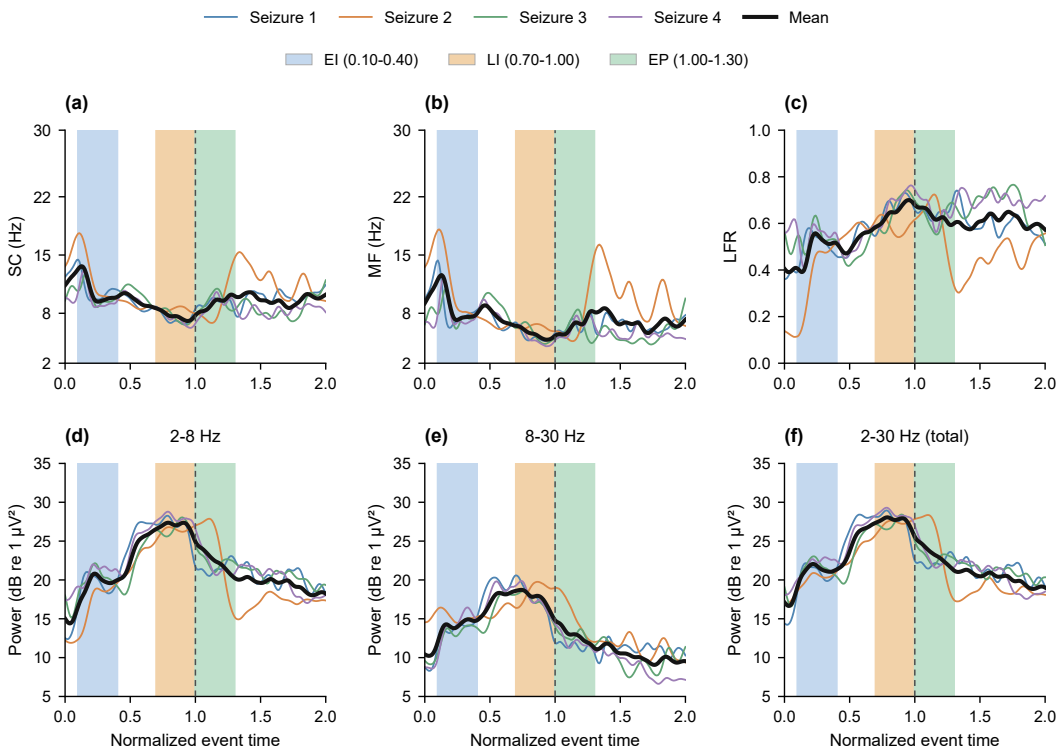


Fig. 3 Relative spectral evolution and absolute-power changes across four PN00 seizures. **(a–c)** Continuous wavelet transform (CWT)-derived spectral centroid (SC), median frequency (MF), and low-frequency ratio (LFR), respectively, calculated over 2–30 Hz. SC and MF are in Hz; LFR is the dimensionless fraction of 2–8 Hz power within 2–30 Hz. **(d–f)** Absolute CWT power within 2–8 Hz, 8–30 Hz, and 2–30 Hz, respectively, expressed in decibels (dB) relative to 1 μV^2. Wavelet normalization and scale weighting are specified in Supplementary Section S2.2. Colored curves show the four passband-compatible seizures, each summarized by the pointwise median across eligible EEG channels; black curves show their within-patient mean. Power is converted to dB before channel and event aggregation. Event colors are consistent across panels. Approximately 10-s Gaussian smoothing is used only for display, not for slope or phase-window calculations. The horizontal axes show normalized event time: 0 denotes onset, 1 the annotated offset, and 2 the end of the duration-matched postictal interval. Dashed vertical lines mark the offset. Blue, orange, and green shaded bands identify the early ictal (EI, 0.10–0.40), late ictal (LI, 0.70–1.00), and early postictal (EP, 1.00–1.30) comparison windows, respectively. Individual-seizure changes and slopes, together with across-seizure variability and confidence intervals for the within-patient mean effects, are reported in Supplementary Table S3.

To distinguish relative spectral redistribution from changes in signal magnitude, we also examined absolute power in these four events (Fig. 3(d–f)). Power within 2–8 Hz increased from the early to the late ictal window in every event, with larger increases in dB than those within 8–30 Hz. During early postictal recovery, both bands and total power were lower than in the late ictal window, although 2–8 Hz power remained above its early ictal level. Thus, the relative shift toward lower frequencies was accompanied by increased low-frequency power during ictal evolution and reduced power in both bands during early postictal recovery.

The above analyses of the PN00 recordings illustrate the fast-to-slow rhythm transition as ictal slowing followed by retained relative low-frequency weighting during early postictal recovery. This pattern links spectral evolution during the seizure to slow activity persisting beyond the annotated offset. For the extended analysis of 33 seizures from 11 patients, seizure-level trajectories were averaged within each patient, with patients serving as the independent statistical units. Ictal SC and MF slopes were more often negative and LFR slopes positive across patients, indicating a tendency toward ictal slowing. However, early

postictal changes differed in direction, with relative low-frequency weighting retained in some patients but not consistently across the cohort. In some patients, early-postictal SC and MF were higher and LFR lower than their early-ictal values. Patient-level SC, MF, and LFR comparisons did not reach significance after multiple-testing correction (Supplementary Section S2.5 and Table S4).

Taken together, these observations identify a clinically observed spectral pattern while highlighting variability in its expression across seizures and patients, motivating a dynamical explanation of the fast-to-slow rhythm transition and its variability. In the following sections, we use the DCE model to investigate how coupled fast and slow processes generate and modulate this spectral evolution within recurrent seizure-like events.

3.2 The DCE model generates the fast-to-slow rhythm transition

The clinical EEG observations in Section 3.1 illustrate a spectral pattern of ictal slowing followed by retained relative low-frequency weighting during early postictal recovery. This spectral pattern provides an empirical reference for the fast-to-slow rhythm transition we aimed to model. Here, we examine how the DCE model can generate a spectral trajectory linking ictal slowing to early postictal slow activity. We first characterize the simulated EEG generated by the DCE model, then illustrate the multi-timescale dynamics responsible for its spectral evolution, and finally introduce model-based definitions of the interictal, ictal, and postictal periods within the DCE framework.

3.2.1 Simulated EEG exhibits a structured fast-to-slow spectral trajectory

Fig. 4(a) shows the simulated EEG generated by the DCE model, which exhibits spontaneous and recurrent seizure-like events separated by intervals of low-amplitude background activity. These events are organized by the ultraslow variable z_1 (Fig. 4(a2), red line) in Subsystem I, whose rise and fall govern the alternation between the active and background states. A representative seizure-like event and its CWT spectrogram are shown in Fig. 4(b). The simulated EEG exhibits a structured waveform evolution during the seizure-like event. Fast ictal-like discharges dominate the early part of the event. As the event progresses, spike-like activity and spike–wave complexes emerge and become increasingly prominent, followed by slow-wave oscillations that dominate the late phase. In parallel, the increasing contribution of slower waveform components shifts spectral power progressively toward lower frequencies, producing a downward spectral trajectory in the spectrogram that qualitatively reproduces the principal spectral dynamics observed in the clinical recordings (Fig. 2(c)). Enlarged waveforms and aligned component trajectories are provided in Supplementary Section S3.1 and Fig. S3(b–d).

The waveform evolution in the simulated EEG reflects the hierarchical organization of three waveform-related timescales in the DCE model. The timescale τ_{x_1} governs the fast ictal discharges generated by Subsystem I, τ_{x_2} governs the spike component of SWDs generated by Subsystem II, and τ_{z_2} governs the slower wave component, with $\tau_{x_1} < \tau_{x_2} \ll \tau_{z_2}$. These three waveform timescales determine the frequency range available to the simulated EEG spectral evolution, whereas the ultraslow timescale τ_{z_1} organizes the recurrence of seizure-like events. Thus, the DCE model embeds a structured waveform evolution within spontaneously recurring events rather than reproducing only a single discharge pattern.

For comparison, we also implemented the original Epileptor model as specified by Jirsa et al. (2014). The model generates recurrent seizure-like events, but its within-event spectral structure remains comparatively stationary and exhibits limited systematic frequency evolution (Supplementary Section S4 and Fig. S4). This qualitative comparison illustrates that the DCE model incorporates additional dynamics that organize spectral evolution within seizure-like events. As shown below, this evolution arises from p-driven transitions among the oscillatory regimes of Subsystem II.

3.2.2 A p-driven oscillatory-regime cascade generates rhythm slowing

To determine how the variable p organizes waveform evolution in the DCE model, we performed

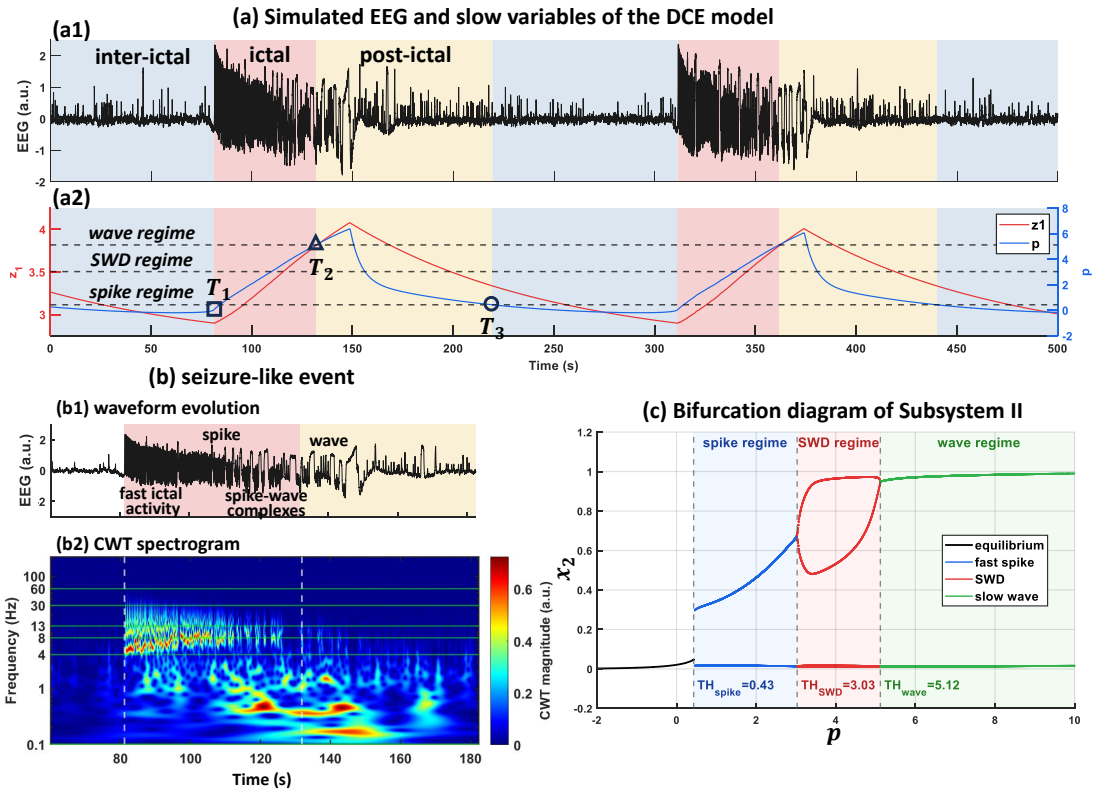


Fig. 4 Simulated fast-to-slow rhythm transition in the DCE model. **(a)** Simulated EEG, $x_1 + 2x_2$, in arbitrary units (a1), and the corresponding ultraslow variable z_1 (red, left axis) and effective drive p (blue, right axis; a2). Blue, pink, and yellow shading denotes model-defined interictal, ictal, and postictal periods, respectively. The open square marks T_1, the local minimum of p preceding sustained increase. The open triangle marks T_2, the upward crossing of $\mathrm{TH}_{\mathrm{wave}}$ by p; the open circle marks T_3, the subsequent downward crossing of $\mathrm{TH}_{\mathrm{spike}}$. **(b)** Enlarged EEG from one event (b1) and its continuous wavelet transform (CWT) spectrogram (b2). Color denotes CWT magnitude in arbitrary units; frequency is in Hz on a logarithmic axis. Vertical dashed lines mark the model-defined ictal boundaries. **(c)** Equilibrium values and local oscillatory maxima and minima of x_2 versus p. Black, blue, red, and green curves denote equilibrium, fast spikes, spike–wave discharges (SWDs), and slow waves, respectively. Dashed lines mark the bifurcation thresholds $\mathrm{TH}_{\mathrm{spike}} = 0.43$, $\mathrm{TH}_{\mathrm{SWD}} = 3.03$, and $\mathrm{TH}_{\mathrm{wave}} = 5.12$, also shown in (a2). Time in (a,b) is expressed in seconds using the rescaling described in Section 2.5. a.u., arbitrary units.

a one-parameter bifurcation analysis of Subsystem II using p as the continuation parameter. The resulting bifurcation diagram of x_2 is shown in Fig. 4(c). Three bifurcation points delimit qualitatively distinct dynamical regimes; we refer to their coordinates along the p-axis as the bifurcation thresholds $\mathrm{TH}_{\mathrm{spike}}$, $\mathrm{TH}_{\mathrm{SWD}}$, and $\mathrm{TH}_{\mathrm{wave}}$. For $p < \mathrm{TH}_{\mathrm{spike}}$, the deterministic subsystem remains at a non-oscillatory equilibrium, although stochastic perturbations in the full DCE model can evoke isolated spike-like events. Above this threshold, Subsystem II exhibits three oscillatory regimes: fast spikes for $\mathrm{TH}_{\mathrm{spike}} < p < \mathrm{TH}_{\mathrm{SWD}}$, SWDs for $\mathrm{TH}_{\mathrm{SWD}} < p < \mathrm{TH}_{\mathrm{wave}}$, and slow waves for $p > \mathrm{TH}_{\mathrm{wave}}$. Under the default parameter setting in Table 1, these bifurcation thresholds are $\mathrm{TH}_{\mathrm{spike}} = 0.43$, $\mathrm{TH}_{\mathrm{SWD}} = 3.03$, and $\mathrm{TH}_{\mathrm{wave}} = 5.12$.

From the perspective of the DCE model, p is not externally prescribed but is controlled by the coupling function $f_2(x_1, z_1)$ defined in Eq. (10). As a seizure-like event evolves, the increase in z_1 and the accumulated low-pass-filtered contribution of x_1 cause p to rise (Fig. 4(a2), blue line). The resulting p trajectory sequentially crosses $\mathrm{TH}_{\mathrm{spike}}$, $\mathrm{TH}_{\mathrm{SWD}}$, and $\mathrm{TH}_{\mathrm{wave}}$, driving Subsystem II from the spike regime through the SWD regime and eventually into the wave regime. This oscillatory-regime cascade progressively increases

the dominant waveform timescale and thereby generates the downward shift of spectral power observed in Fig. 4(b2).

Because p is constructed from both z_1 and the filtered fast activity x_1, the oscillatory-regime cascade is endogenously embedded within the recurrent seizure dynamics organized by Subsystem I. Therefore, the ultraslow variable z_1 organizes when seizure-like events arise, whereas p organizes how their waveform and spectrum evolve within each event. Although the simulated EEG is read out as the linear combination $x_1 + 2x_2$, the two components are generated by nonlinearly coupled rather than independent dynamics. The fast-to-slow spectral trajectory therefore cannot be attributed to a simple superposition of independently generated fast and slow oscillations.

3.2.3 Interictal–ictal–postictal cycle in the DCE model

The clinical example in Fig. 2(c) shows ictal slowing followed by persistent low-frequency activity beyond the annotated seizure offset. To relate these successive spectral features within the DCE framework, we define model-based interictal, ictal, and postictal periods from the p trajectory, as shown in Fig. 4(a2), where the oscillatory-regime thresholds are taken from Fig. 4(c).

Because each rise in z_1 initiates a new seizure-like event and is accompanied by an almost simultaneous rise in p (Eq. (10), p depends linearly on z_1), we define *the onset of the ictal period* as the moment when p begins to increase (T_1, marked by the open square in Fig. 4(a2)). During the interval following T_1, the oscillatory activity gradually slows as p continuously increases. Motivated by the persistence of low-frequency activity after the annotated offset in the clinical example (Fig. 2(c)), we define *the onset of the postictal period* as the moment when p exceeds the wave-regime threshold $\mathrm{TH}_{\mathrm{wave}}$ (T_2, marked by the open triangle). Accordingly, the interval (T_1, T_2) is defined as the *ictal period*. After T_2, p continues to increase for a short duration, maintaining the slow-wave regime. Subsequently, as z_1 decreases and the simulated EEG returns toward low-amplitude background activity, p also begins to decrease. We define *the onset of the interictal period* as the moment when p returns below the spike-regime threshold $\mathrm{TH}_{\mathrm{spike}}$ (T_3, marked by the open circle). The interval (T_2, T_3) is therefore defined as the *postictal period*. Together, these definitions establish a complete interictal–ictal–postictal cycle in the DCE model.

It should be noted that during the model-defined postictal period (T_2, T_3), the effective drive p subsequently declines from the wave regime through the SWD and spike regimes. Passage through the spike regime permits transient spike-like activity before p falls below $\mathrm{TH}_{\mathrm{spike}}$ and Subsystem II returns to the non-oscillatory regime. We describe this recovery activity as postictal spikes in the model, qualitatively consistent with reports of residual spikes after clinical seizure termination (Pottkamper et al. 2020). Enlarged waveforms illustrating these spikes are provided in Supplementary Section S3.1 and Fig. S3(d3). Moreover, further analysis of the coupling dynamics, including the modulation of the Subsystem I oscillation envelope by Subsystem II, is provided in Supplementary Section S3.2.

In summary, the DCE model generates the fast-to-slow rhythm transition through a hierarchy of waveform timescales and an endogenous p-driven cascade across spike, SWD, and wave regimes. Coupling the p dynamics to the ultraslow, z_1-driven seizure cycle embeds this event-level spectral evolution within a long-term interictal–ictal–postictal cycle. In the following section, we examine how distinct parameter families control the spectral span, temporal organization, and oscillatory-regime composition of this rhythm transition.

3.3 Parameter-to-phenotype decomposition of the fast-to-slow rhythm transition

In Section 3.2, we showed that the DCE model reproduces the fast-to-slow rhythm transition via p-driven oscillatory-regime transitions in Subsystem II. Although this transition is generated by the same underlying mechanism, clinical heterogeneity across patients and seizures can produce variation in its spectral and temporal features. We therefore asked how such variability is organized in the parameter space of the DCE model. We decomposed the rhythm transition into three phenotypic dimensions—spectral span, temporal organization, and oscillatory-regime composition—and investigated how these

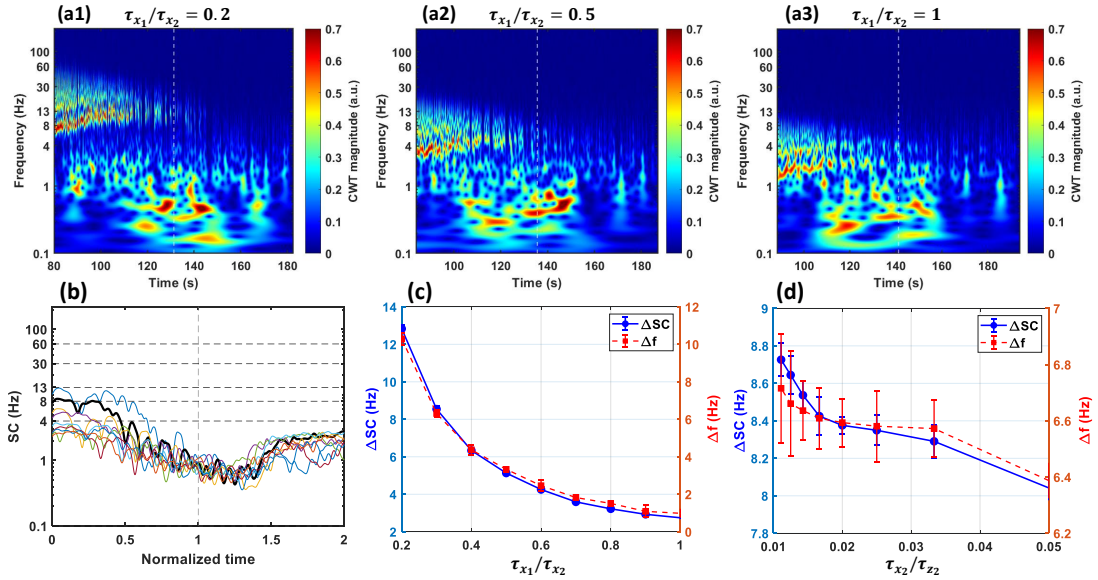


Fig. 5 Effects of timescale separation on the spectral span of simulated rhythm transitions. **(a1–a3)** Continuous wavelet transform (CWT) spectrograms at $\tau_{x_1}/\tau_{x_2} = 0.2$, 0.5, and 1, respectively, with $\tau_{x_2} = 1$ fixed. From left to right, decreasing timescale separation makes the high- and low-frequency components less clearly separated, resulting in a less distinct fast-to-slow spectral transition. Color bars show CWT magnitude in arbitrary units (a.u.) on a common scale. Frequency is in Hz on logarithmic axes. Vertical dashed lines mark the model-defined ictal–postictal boundary. **(b)** Spectral centroid (SC) trajectories for the examined values of τ_{x_1}/τ_{x_2}, displayed in Hz on a logarithmic vertical axis. Colored curves denote different ratios; the bold black curve denotes the default ratio of 0.3. Normalized times 0, 1, and 2 mark ictal onset, the ictal–postictal boundary, and the end of the analyzed postictal interval, respectively. **(c,d)** Spectral-span measures versus τ_{x_1}/τ_{x_2} and τ_{x_2}/τ_{z_2}, respectively. Blue circles (left axis) show $\Delta\mathrm{SC} = \max(\mathrm{SC}) - \min(\mathrm{SC})$; red squares (right axis) show the onset-to-end mean-frequency difference, $\Delta f = f_{\mathrm{onset}} - f_{\mathrm{end}}$, defined in Section 3.3.1. Both measures are in Hz; markers and error bars denote means and standard deviations across detected seizure-like events. Note that the vertical scale in panel (d) is substantially smaller than that in panel (c).

dimensions are controlled by distinct parameter families within the DCE model.

3.3.1 Timescale separation controls spectral span

The first dimension—the spectral span of the rhythm transition—is governed by the degree of separation among the model's intrinsic timescales. As introduced in Section 2, a defining feature of the DCE model is its multi-timescale structure. Three waveform-related timescale parameters are τ_{x_1}, τ_{x_2}, and τ_{z_2}, satisfying $\tau_{x_1} < \tau_{x_2} < \tau_{z_2}$. Specifically, τ_{x_1} governs the timescale of fast ictal discharges, while τ_{x_2} and τ_{z_2} govern the fast-spike and slow-wave components of SWDs, respectively. Together, these parameters define the spectral bandwidth available to the rhythm transition. Here, we examined how the degree of separation among these timescales shaped the time–frequency structure of the rhythm transition. Specifically, we fixed $\tau_{x_2} = 1$ and focused on two ratios: τ_{x_1}/τ_{x_2} and τ_{x_2}/τ_{z_2}.

The spectrograms of seizure-like events generated at different values of τ_{x_1}/τ_{x_2} are shown in Fig. 5(a1–a3). When the timescale separation is pronounced ($\tau_{x_1}/\tau_{x_2} = 0.2$; Fig. 5(a1)), the spectrogram exhibits two well-separated spectral components: an early high-frequency band and a late low-frequency band, with a clear gap between them that reflects the orderly transition from fast to slow rhythmic activity. As τ_{x_1}/τ_{x_2} increases, the two components progressively overlap. When $\tau_{x_1}/\tau_{x_2} = 1$ (Fig. 5(a3)), the transition becomes less separable and appears as a broadband oscillatory event. To quantify this effect, we computed the SC trajectories across different τ_{x_1}/τ_{x_2} values (Fig. 5(b)). At seizure onset, the trajectories are highly divergent, with smaller ratios corresponding to higher initial SC values. Although the trajectories originate from markedly different

initial SC values, they converge toward a similar low-frequency endpoint during seizure evolution and postictal recovery. This convergence indicates that τ_{x_1} primarily determines the upper spectral bound of the rhythm transition. Fig. 5(c) summarizes the dependence of the spectral span on τ_{x_1}/τ_{x_2}. Both $\Delta\mathrm{SC} = \max(\mathrm{SC}) - \min(\mathrm{SC})$ and the onset-to-end frequency difference $\Delta f = f_{\mathrm{onset}} - f_{\mathrm{end}}$ decrease monotonically as τ_{x_1}/τ_{x_2} approaches 1, where f_{onset} and f_{end} are the mean frequency over the first and last 5% of the ictal–postictal time window, respectively. The decline is steeper where the timescale separation is larger (lower τ_{x_1}/τ_{x_2}), indicating that the spectral span is sensitive to changes in the degree of separation when the two timescales are far apart.

Whereas τ_{x_1} determines the upper spectral bound, the slow timescale τ_{z_2} determines the lower bound. As shown in Fig. 5(d), we varied τ_{z_2} and evaluated $\Delta\mathrm{SC}$ and Δf as functions of τ_{x_2}/τ_{z_2}. As τ_{z_2} decreases (i.e., τ_{x_2}/τ_{z_2} increases), the low-frequency band of the slow-wave component shifts upward, compressing the spectral span from below. Consequently, both $\Delta\mathrm{SC}$ and Δf decrease with increasing τ_{x_2}/τ_{z_2}. It should be noted that the decline of $\Delta\mathrm{SC}$ and Δf in Fig. 5(d) is more gradual than that in Fig. 5(c). This difference arises because, with $\tau_{x_2} = 1$ fixed, the examined values of τ_{z_2} are considerably larger than those of τ_{x_1}, making the ratio τ_{x_2}/τ_{z_2} vary over a much narrower relative range than τ_{x_1}/τ_{x_2}. Hence, within the parameter ranges examined here, the spectral span appears more sensitive to variations in τ_{x_1} than in τ_{z_2}.

Taken together, the degree of timescale separation, quantified by the ratios τ_{x_1}/τ_{x_2} and τ_{x_2}/τ_{z_2}, determines the spectral span of the rhythm transition, with the upper and lower spectral bounds controlled by the fastest and the slowest waveform timescales, τ_{x_1} and τ_{z_2}, respectively. These results suggest that the spectral span of the transition is set by the hierarchical timescale organization of the DCE model.

3.3.2 Filtering rates control temporal organization

Section 3.3.1 established that timescale ratios set the spectral bandwidth within which the rhythm transition unfolds. We next examined the second phenotypic dimension, the temporal organization of this transition, which is controlled by the filtering rate constants γ_1 and γ_2 introduced in Section 2.4. These parameters govern the rates at which the slow variable p rises during ictal buildup and decays during postictal recovery. As illustrated in Fig. 6(a), increasing γ_1 (panel (a2)) relative to the default value (panel (a1)) accelerates the rise of p, causing it to reach the $\mathrm{TH}_{\mathrm{wave}}$ more rapidly. Conversely, decreasing γ_2 (panel (a3)) slows the decay of p, delaying its return below the $\mathrm{TH}_{\mathrm{spike}}$. Here, we systematically varied γ_1 and γ_2 to dissect their respective roles in shaping the temporal organization of the ictal–postictal cycle.

We first varied γ_1 while holding $\gamma_2 = 0.015$ fixed. For each parameter combination, we ran the DCE model, detected seizure-like events using the z_1- and p-based criteria described in Section 3.2.3, and extracted the ictal duration $(T_2 - T_1)$ and postictal duration $(T_3 - T_2)$. As shown in Fig. 6(b), the ictal duration decreases monotonically with increasing γ_1, consistent with the expectation that faster filtering accelerates p accumulation. However, the total ictal–postictal cycle duration remains nearly constant, implying a corresponding increase in postictal duration. This behavior can be understood from the role of z_1. Because the overall cycle structure of the DCE model is governed by z_1, whose dynamics are independent of γ_1, the moment at which p begins to decrease (i.e., the moment at which z_1 begins to decrease) remains approximately fixed. Consequently, an earlier T_2 does not simply shorten the ictal phase; it reallocates a portion of the fixed ictal–postictal window from the ictal to the postictal phase, without substantially changing the overall cycle duration. We next varied γ_2 while holding $\gamma_1 = 0.001$ fixed. As shown in Fig. 6(c), the postictal duration decreases monotonically as γ_2 increases, whereas the ictal duration remains nearly constant. This is because T_2 is determined by γ_1 before γ_2 becomes operative; the total ictal–postictal cycle duration therefore shortens as postictal recovery accelerates. These results identify γ_2 as a dedicated regulator of postictal recovery: it controls the speed of postictal recovery without affecting the ictal phase.

Since γ_1 and γ_2 control opposite phases of the ictal–postictal cycle, a natural question is whether their combined effect can be captured by a single asymmetry parameter. To explore this,

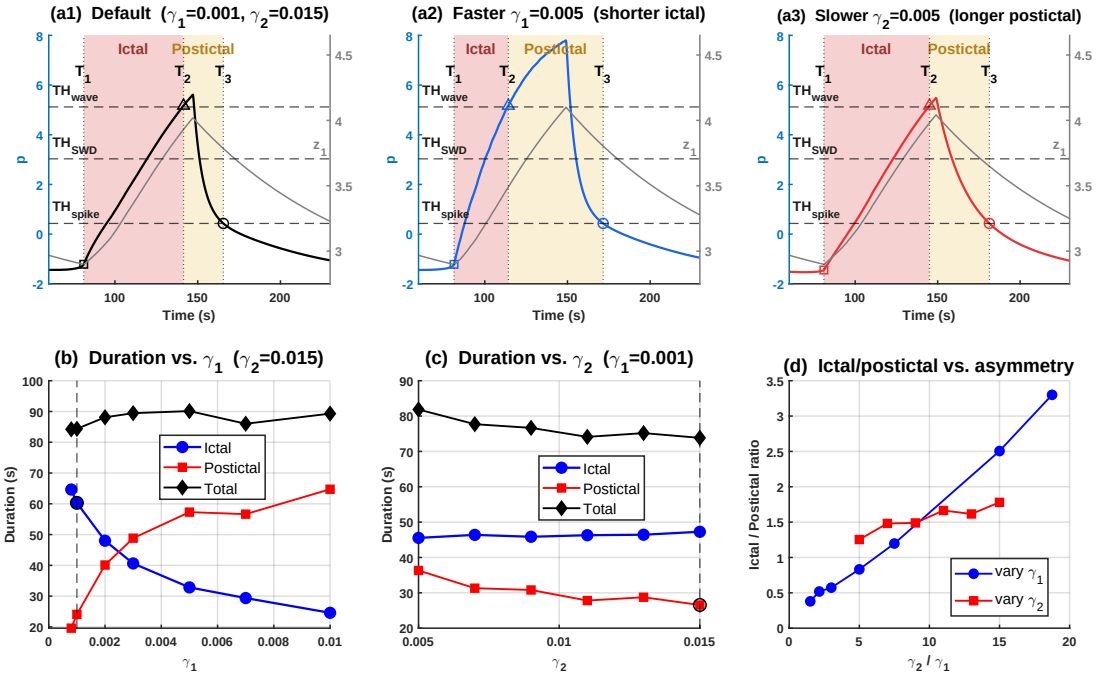


Fig. 6 Effects of filtering rates on model-defined ictal and postictal durations. **(a1–a3)** Effective drive p (black, blue, and red, respectively; left axis) and ultraslow variable z_1 (gray; right axis). Panel (a1) uses the default filtering rates, $\gamma_1 = 0.001$ and $\gamma_2 = 0.015$. Relative to this reference, panel (a2) increases γ_1 to 0.005 while keeping γ_2 unchanged, accelerating the rise of p and shortening the ictal period. Panel (a3) decreases γ_2 to 0.005 while keeping γ_1 unchanged, slowing the decay of p and prolonging the postictal period. Pink and yellow shading denotes ictal and postictal periods. Open squares, triangles, and circles mark T_1 (onset of sustained p increase), T_2 (upward wave-threshold crossing), and T_3 (subsequent downward spike-threshold crossing), respectively. Horizontal dashed lines mark $\mathrm{TH_{spike}} = 0.43$, $\mathrm{TH_{SWD}} = 3.03$, and $\mathrm{TH_{wave}} = 5.12$; SWD denotes spike–wave discharge. **(b,c)** Ictal duration $T_2 - T_1$ (blue circles), postictal duration $T_3 - T_2$ (red squares), and their sum (black diamonds) versus γ_1 and γ_2, respectively. The other rate is fixed at its default value. Vertical dashed lines indicate the default rates. **(d)** Ictal-to-postictal duration ratio, $(T_2 - T_1)/(T_3 - T_2)$, versus the filtering-rate ratio γ_2/γ_1. The curves are calculated from the γ_1 sweep in panel (b) (blue circles) and the γ_2 sweep in panel (c) (red squares).

we plotted the ictal-to-postictal ratio against the parameter ratio γ_2/γ_1 in Fig. 6(d), using the data from Fig. 6(b,c) on a common axis. Two features are noteworthy. First, both curves show an overall increasing trend: increasing γ_2/γ_1—whether by decreasing γ_1 or increasing γ_2—increases the ictal/postictal ratio. Second, the two curves exhibit markedly different slopes: the curve obtained by varying γ_1 is steep, whereas the curve obtained by varying γ_2 is shallow. Consequently, parameter pairs (γ_1, γ_2) with the same ratio γ_2/γ_1 can nevertheless produce substantially different temporal compositions of the ictal–postictal cycle. This divergent behavior underscores that γ_1 and γ_2 are functionally independent parameters whose effects cannot be reduced to a single asymmetry measure.

Taken together, the two filtering rate constants provide independent control over distinct temporal aspects of the rhythm transition. Specifically, γ_1 determines how rapidly the fast-to-slow rhythm transition proceeds and thereby influences the temporal partitioning of the ictal–postictal cycle, whereas γ_2 primarily regulates the duration of postictal recovery without substantially affecting ictal evolution. This separation of functions enables the DCE model to independently tune seizure evolution and postictal dynamics, thereby providing a model mechanism for generating temporal variability in the rhythm transition.

3.3.3 Bifurcation thresholds control oscillatory-regime composition

The third phenotypic dimension, the composition of oscillatory regimes, is shaped by the locations of the bifurcation thresholds $\mathrm{TH_{spike}}$, $\mathrm{TH_{SWD}}$, and $\mathrm{TH_{wave}}$ in p-space. As p drives Subsystem II through the spike, SWD, and wave

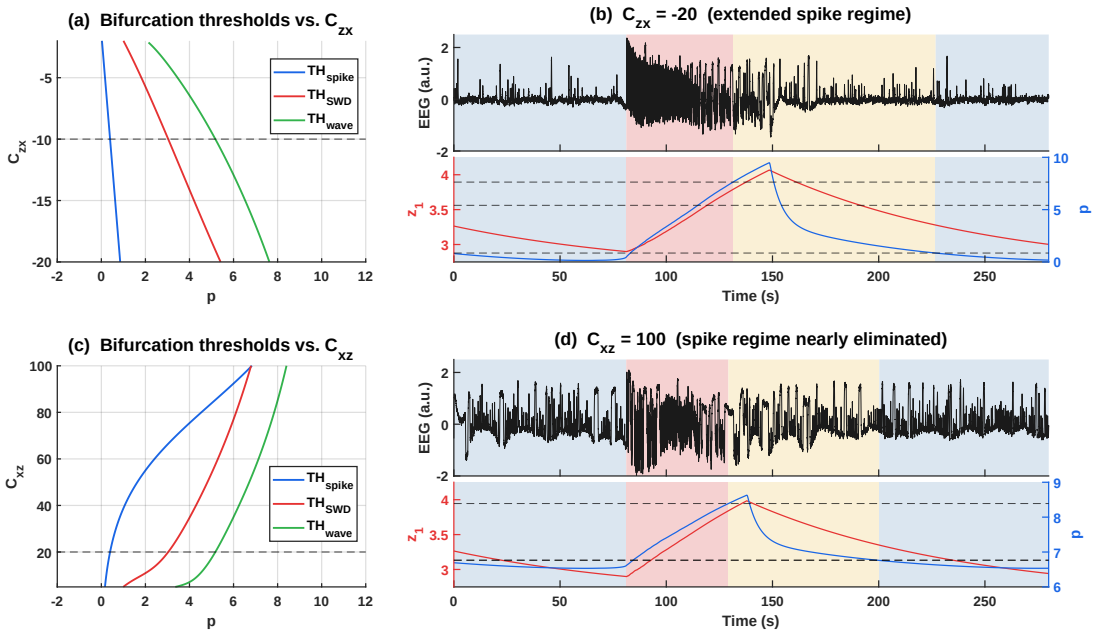


Fig. 7 Cross-timescale coupling controls bifurcation thresholds and oscillatory-regime composition in Subsystem II. **(a,c)** Two-parameter bifurcation diagrams in the (p, C_{zx}) and (p, C_{xz}) planes, respectively. Blue, red, and green curves locate the spike, spike–wave discharge (SWD), and wave thresholds, $\mathrm{TH}_{\mathrm{spike}}$, $\mathrm{TH}_{\mathrm{SWD}}$, and $\mathrm{TH}_{\mathrm{wave}}$. Horizontal dashed lines mark the default values $C_{zx} = -10$ and $C_{xz} = 20$. Increasing $|C_{zx}|$ widens the spike regime, whereas increasing C_{xz} narrows it. **(b,d)** Simulations at $C_{zx} = -20$ and $C_{xz} = 100$, respectively, with the other coupling coefficient at its default value. Upper traces show the simulated EEG, $x_1 + 2x_2$, in arbitrary units (a.u.). Lower traces show z_1 (red, left axis) and p (blue, right axis). Panel (b) illustrates an extended spike-dominated interval; panel (d) illustrates the near-merger of the spike and SWD thresholds. Dashed horizontal lines in the lower plots mark the corresponding oscillatory-regime thresholds. Blue, pink, and yellow shading denotes model-defined interictal, ictal, and postictal periods, respectively.

regimes, these thresholds shape the relative occupancy and availability of each oscillatory regime during the rhythm transition. To examine how cross-timescale coupling modulates these thresholds, we performed two-parameter continuation analyses in the (p, C_{zx}) and (p, C_{xz}) planes. These two parameters were selected because they form the reciprocal coupling between the fast variable x_2 and the slow variable z_2 (Eqs. (6) and (8)) in Subsystem II and are therefore directly relevant to the cross-timescale interactions underlying SWD dynamics.

Fig. 7(a) shows the dependence of the three thresholds on C_{zx}. All three thresholds increase approximately linearly with $|C_{zx}|$, but with markedly different slopes. $\mathrm{TH}_{\mathrm{spike}}$ is nearly insensitive to C_{zx}: before Subsystem II enters the spike regime, z_2 remains close to zero, rendering the inhibitory term $C_{zx} \cdot z_2$ in Eq. (6) negligible regardless of the value of C_{zx}. By contrast, $\mathrm{TH}_{\mathrm{SWD}}$ and $\mathrm{TH}_{\mathrm{wave}}$ are strongly modulated by C_{zx}: by the time p approaches the SWD threshold, the slow variable z_2 is fully activated, and the inhibitory term $C_{zx} \cdot z_2$ constitutes a substantial negative contribution to the net input in Eq. (6). Stronger inhibition (larger $|C_{zx}|$) therefore demands a larger p to overcome this suppression, shifting $\mathrm{TH}_{\mathrm{SWD}}$ and $\mathrm{TH}_{\mathrm{wave}}$ to higher values. As a result of this differential sensitivity, increasing $|C_{zx}|$ selectively expands the spike regime while leaving the SWD regime largely unchanged. From the perspective of the rhythm transition, a wider spike regime requires a larger increment of p to reach the SWD regime, leading to an extended spike-dominated phase before organized spike–wave complexes emerge (Fig. 7(b)). Conversely, reducing $|C_{zx}|$ allows spike–wave complexes to appear at lower p, compressing the spike phase.

Fig. 7(c) shows the dependence on C_{xz}. Since C_{xz} and C_{zx} correspond to functionally opposite connections in Subsystem II, Fig. 7(c) exhibits an overall trend opposite to that of Fig. 7(a): all three thresholds increase with C_{xz}. The parameter C_{xz}

mainly affects the width of the spike regime, with a relatively weak influence on the width of the SWD regime. Notably, as C_{xz} increases, $\mathrm{TH}_{\mathrm{spike}}$ rises at an accelerating rate. At $C_{xz} \approx 100$, $\mathrm{TH}_{\mathrm{spike}}$ and $\mathrm{TH}_{\mathrm{SWD}}$ merge, eliminating the intermediate spike regime altogether, and the system transitions directly from the quiescent state into SWD upon crossing the merged threshold. From the perspective of the rhythm transition, this represents an extreme case in which spike–wave complexes appear immediately at seizure onset, with no preceding large-amplitude spikes (Fig. 7(d)). Taken together, the bifurcation structure of Subsystem II determines the temporal allocation of oscillatory regimes during the rhythm transition. By shifting the boundaries between oscillatory regimes, C_{zx} and C_{xz} regulate not only the relative proportion of each regime but also whether a given regime is expressed.

Overall, Sections 3.3.1–3.3.3 establish a three-dimensional parameter-to-phenotype mapping for the DCE model. These dimensions, although parameterized independently, jointly shape the observable fast-to-slow rhythm transition: timescale ratios define the spectral range over which the transition can unfold, bifurcation thresholds partition the p-trajectory into regime-specific intervals, and filtering rates determine how rapidly the system traverses these intervals. This decomposition provides a compact framework for understanding how the DCE model can generate diverse rhythm-transition patterns from a common dynamical architecture.

3.4 Coupled DCE nodes: recruitment-induced rhythm transitions

The analyses above focused on an isolated, intrinsically epileptogenic DCE model ($z_0 < 2.95$), in which fast-to-slow rhythm transitions arise together with spontaneous seizure-like events. In the epileptic brain, however, seizure activity can propagate across cortical regions and recruit initially non-epileptogenic tissue into ictal dynamics (Proix et al. 2018). We therefore extended the analysis to two coupled DCE nodes and asked: when an epileptogenic node drives a non-epileptogenic node into a seizure via inter-node coupling, does the recruited seizure exhibit the same fast-to-slow rhythm transition as the spontaneously generated one? To investigate this, we constructed a two-node coupled system in which two DCE models, denoted Node 1 and Node 2, interact through their ultraslow variables $z_1^{(1)}$ and $z_1^{(2)}$. The state equation for z_1 (Eq. (3)) was modified to incorporate an inter-node coupling term, as follows:

$$\begin{aligned}\frac{dz_1^{(i)}}{dt} = \frac{1}{\tau_{z_1}}\Big[&-z_1^{(i)} + h(x_1^{(i)}; z_0^{(i)}) \\ &+ K \cdot (x_1^{(i)} - x_1^{(j)})\Big], \\ &i, j \in \{1, 2\},\ i \neq j,\end{aligned} \tag{12}$$

where $z_1^{(i)}$ and $x_1^{(i)}$ are state variables of Node i, $z_0^{(i)}$ sets its epileptogenicity, and $K > 0$ is the inter-node coupling strength.

3.4.1 Recruitment mode map

We first constructed a recruitment mode map for the two coupled DCE nodes and clarified the dynamical mechanism encoded by the coupling term in Eq. (12). Node 1 was set to high epileptogenicity ($z_0^{(1)} = 2.6$) to generate spontaneous seizures, whereas Node 2 was configured to be non-epileptogenic ($z_0^{(2)} \geq 2.95$) so that seizure activity in Node 2 could emerge only via recruitment. We performed simulations across a broad grid of $(z_0^{(2)}, K)$ parameter combinations and categorized the resulting recruitment dynamics. As shown in Fig. 8(a), four qualitatively distinct recruitment modes emerged within the $(z_0^{(2)}, K)$ parameter plane:

- **One-to-one entrainment**: Seizure events in the two nodes are quasi-synchronized; each seizure in Node 1 reliably triggers a corresponding seizure in Node 2.
- **Many-to-one recruitment**: Two or more successive seizures in Node 1 are required to initiate a single seizure in Node 2.
- **No recruitment**: Discharges from Node 1 cannot trigger any seizure activity in Node 2.
- **Suppression**: Node 1 not only fails to recruit Node 2, but is itself suppressed by Node 2; consequently, neither node generates seizure activity.

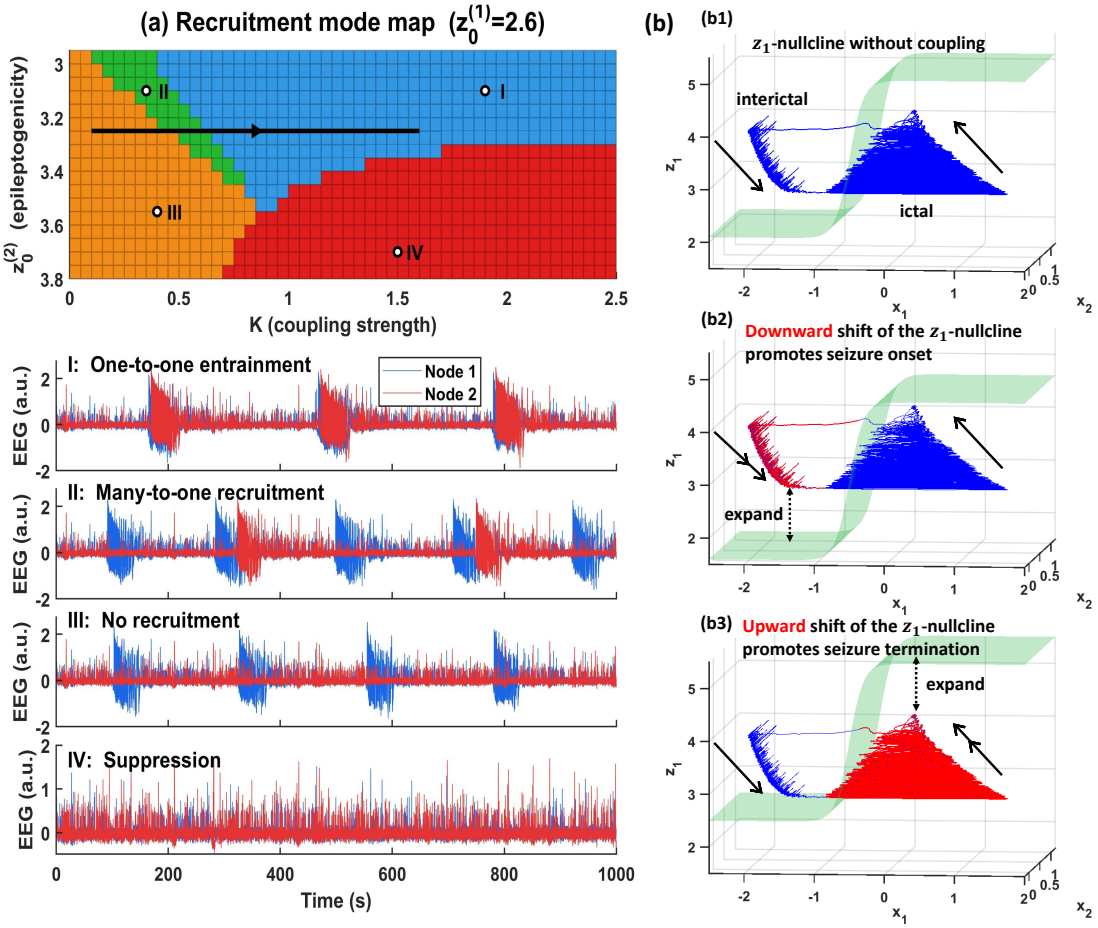


Fig. 8 Recruitment modes and coupling-induced nullcline shifts in two coupled DCE nodes. **(a)** Recruitment-mode map versus coupling strength K and Node 2 epileptogenicity parameter $z_0^{(2)}$, with $z_0^{(1)} = 2.6$ fixed. Colors in the $(K, z_0^{(2)})$ parameter plane identify four recruitment modes: one-to-one entrainment (I, blue), many-to-one recruitment (II, green), no recruitment (III, orange), and suppression (IV, red). Open circles identify parameter combinations for the EEG traces below (Node 1, blue; Node 2, red). The black arrow marks the path $z_0^{(2)} = 3.25$ analyzed in Sections 3.4.2 and 3.4.3. a.u., arbitrary units. **(b)** State trajectories and z_1-nullclines ($dz_1/dt = 0$, green surfaces) in the (x_1, x_2, z_1) state space. Panel (b1) shows the uncoupled reference. A downward nullcline shift accelerates interictal z_1 decay and promotes seizure onset (b2); an upward shift accelerates ictal z_1 increase and promotes termination (b3). Red trajectory segments highlight the affected portions relative to the blue reference. Double arrows indicate faster z_1 evolution than single arrows; dotted double-headed arrows indicate the enlarged separation from the shifted nullcline.

These four modes occupy contiguous domains in the $(z_0^{(2)}, K)$ parameter plane, collectively forming the recruitment mode map. Notably, when the coupling strength K is sufficiently large, only one-to-one entrainment and suppression are accessible, both of which are characterized by convergence of the two nodes' seizure dynamics toward a common pattern. This convergence is qualitatively consistent with clinical observations of increased synchronization within epileptic networks (Bartolomei et al. 2004). The coupling formulation in Eq. (12) embodies this network homogenization principle at the timescale of the ultraslow homeostatic variable z_1. In detail, the coupling term $K \cdot (x_1^{(i)} - x_1^{(j)})$ dynamically shifts the z_1-nullcline ($dz_1/dt = 0$) of each node, generating a driving force that pushes each node's discharge state toward that of the other.

To illustrate the dynamics introduced by the coupling term, we consider a representative scenario in which Node 1 is in the ictal state (elevated $x_1^{(1)}$, rising $z_1^{(1)}$) whereas Node 2 is in the interictal state (suppressed $x_1^{(2)}$, falling $z_1^{(2)}$). The

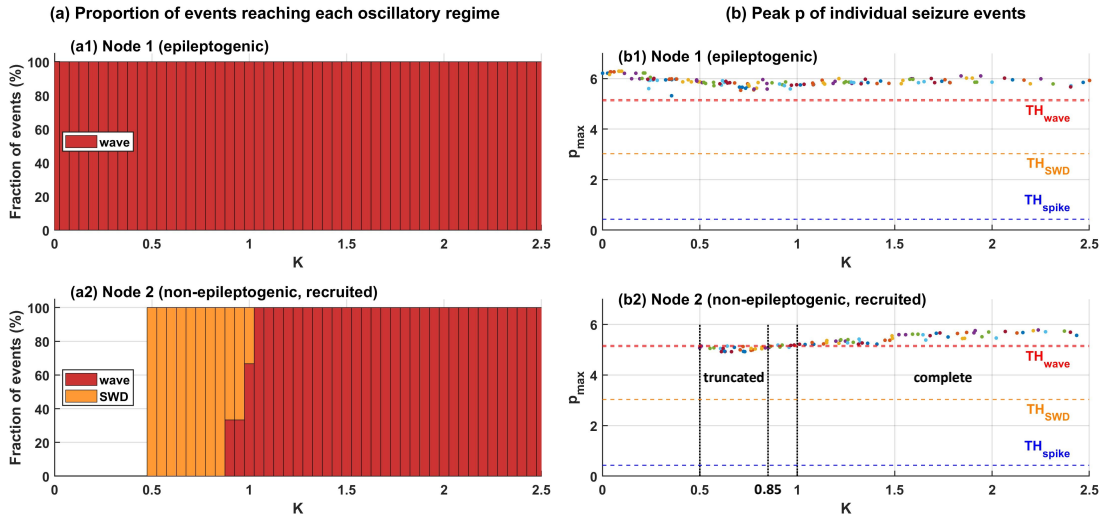


Fig. 9 Coupling-dependent recruitment of slow-wave activity in two model nodes. **(a)** Percentages of detected seizure-like events classified by the highest oscillatory regime reached by the effective drive p. Orange bars denote events reaching the spike–wave discharge (SWD) regime, $\mathrm{TH_{SWD}} < p_{\max} < \mathrm{TH_{wave}}$; red bars denote events reaching the wave regime, $p_{\max} > \mathrm{TH_{wave}}$. Panels (a1,a2) show the driving Node 1 and recruited Node 2, respectively, with $z_0^{(1)} = 2.6$ and $z_0^{(2)} = 3.25$. Each percentage uses the detected events at the corresponding coupling strength K as its denominator; blank regions indicate no detected events. **(b)** Peak drive $p_{\max}$ for individual events in Node 1 (b1) and Node 2 (b2). Each point denotes one event. Horizontal dashed lines mark $\mathrm{TH_{spike}} = 0.43$ (blue), $\mathrm{TH_{SWD}} = 3.03$ (orange), and $\mathrm{TH_{wave}} = 5.12$ (red). Vertical dotted lines in (b2) separate truncated transitions ($0.5 \le K < 0.85$), coexistence of truncated and complete transitions ($0.85 \le K < 1$), and complete transitions ($K \ge 1$). Complete transitions reach the wave regime; truncated transitions do not.

relationship between the two discharge states and the z_1-nullcline in state space is illustrated in Fig. 8(b1). (For clarity, we do not distinguish between interictal and postictal states in this nullcline analysis.) From the perspective of Node 2, the coupling term $K \cdot (x_1^{(2)} - x_1^{(1)})$ is negative, which shifts the $z_1^{(2)}$-nullcline downward (Fig. 8(b2)), accelerates the interictal decay of $z_1^{(2)}$, and thereby promotes seizure onset. Conversely, the coupling term $K \cdot (x_1^{(1)} - x_1^{(2)})$ is positive for Node 1, which shifts its $z_1^{(1)}$-nullcline upward (Fig. 8(b3)) and thereby promotes seizure termination. Overall, the inter-node coupling exerts a *balancing, convergence-promoting* effect that drives the discharge states of the two nodes to converge. At sufficiently strong coupling, this convergent effect becomes dominant, locking both nodes into unified seizure dynamics, as observed in the one-to-one entrainment or suppression regimes on the right side of the recruitment mode map.

3.4.2 Coupling strength determines whether recruited rhythm transitions reach the slow-wave regime

The recruitment mode map in Fig. 8(a) illustrates how a non-epileptogenic Node 2 can be driven to generate seizure activity by an epileptogenic Node 1, and classifies distinct recruitment patterns based on node epileptogenicity and inter-node coupling strength. We then examined whether the recruited seizures in Node 2 exhibited the same fast-to-slow rhythm transition as the spontaneous seizures of Node 1. To do so, we fixed Node 2's epileptogenicity at $z_0^{(2)} = 3.25$ (the parameter path marked by the black arrow in Fig. 8(a)) and swept the coupling strength K over the interval $[0, 2.5]$, covering the full trajectory from no recruitment to stable one-to-one entrainment. For each value of K, we detected all seizure events in both nodes, extracted the peak value of the slow variable p within each seizure window, and classified each event according to the highest oscillatory-regime threshold ($\mathrm{TH_{spike}}$, $\mathrm{TH_{SWD}}$, or $\mathrm{TH_{wave}}$) reached by its $p_{\max}$.

We first quantified how far rhythm slowing progressed within each seizure event. We refer to this property as *rhythm transition completeness*: a transition is classified as complete when $p_{\max} > \mathrm{TH}_{\mathrm{wave}}$ and the event expresses the full spike-to-SWD-to-wave sequence. A transition is classified as truncated when $p_{\max}$ remains below $\mathrm{TH}_{\mathrm{wave}}$, such that slow-wave activity is absent. As illustrated in Fig. 9(a,b), Node 1 and Node 2 exhibit markedly different degrees of rhythm transition completeness as coupling strength varies. The epileptogenic Node 1 exhibits complete three-regime rhythm transitions ($p_{\max} > \mathrm{TH}_{\mathrm{wave}}$) for all seizures across the entire range of K (Fig. 9(a1)), with only a mild reduction in $p_{\max}$ as K initially increases (Fig. 9(b1)). In contrast, the rhythm transition completeness of the recruited Node 2 displays a pronounced dependence on K (Fig. 9(a2)):

- **Truncated rhythm transition ($0.5 \leq K < 0.85$):** Node 2 is recruited to generate seizures, but each recruited seizure reaches only the SWD regime ($\mathrm{TH}_{\mathrm{SWD}} < p_{\max} < \mathrm{TH}_{\mathrm{wave}}$). The recruitment-induced rhythm transition is therefore truncated: spike–wave complexes appear, whereas the slow-wave oscillatory component is absent.
- **Coexistence of truncated and complete transitions ($0.85 \leq K < 1$):** Node 2 gradually produces recruited seizures that extend into the wave regime ($p_{\max} > \mathrm{TH}_{\mathrm{wave}}$), and the proportion of such complete events increases with K.
- **Complete rhythm transition ($1 \leq K \leq 2.5$):** All recruited seizures in Node 2 reach the wave regime, producing complete three-regime transitions whose oscillatory composition matches that of spontaneous seizures in Node 1.

Consistent with this coupling-dependent progression toward slow-wave activity, $p_{\max}$ in Node 2 increases from below to above $\mathrm{TH}_{\mathrm{wave}}$ as K increases (Fig. 9(b2)). This trend is opposite to the slight $p_{\max}$ reduction observed in Node 1 (Fig. 9(b1)), further reflecting the balancing, convergence-promoting effect of the coupling term in Eq. (12). As coupling increases, recruited transitions progress from the SWD regime into the wave regime, making their oscillatory composition increasingly similar to that of spontaneous seizures in the driving node. The inter-node coupling therefore promotes convergence not only in macroscopic seizure synchronization but also in the fine-grained oscillatory composition within individual seizure events.

3.4.3 Recruited events exhibit longer model-defined postictal durations

Having established that coupling strength determines how far recruited rhythm transitions progress toward slow-wave activity, we next examined model-defined postictal duration. Given that the $p_{\max}$ of a truncated rhythm transition is lower than that of a complete one, one might expect recruited seizures with truncated transitions to have a shorter postictal duration than spontaneous seizures. Simulations reveal the opposite trend. Fig. 10(a) shows the simulated EEG and p trajectories for the two DCE nodes at $K = 0.8$. For the truncated rhythm transition in Node 2, whose $p^{(2)}_{\max}$ does not cross $\mathrm{TH}_{\mathrm{wave}}$, we define the onset of the postictal period as the moment when p begins to decrease. Even though these recruited events in Node 2 lack the wave regime, their postictal recovery duration is markedly longer than that of the spontaneous seizures in Node 1. Moreover, as shown in Fig. 10(b), the postictal periods of recruited seizures in Node 2 remain consistently longer than those of spontaneous seizures in Node 1 across the full range of K, even when both nodes exhibit complete rhythm transitions under strong coupling.

This systematic difference in postictal duration is associated with the delay between the two nodes' seizure-termination times. Comparison of the EEG traces in Fig. 10(a1,a2) shows that when Node 1's seizure terminates, Node 2's seizure is still ongoing. During the interval $(T_2^{(1)}, T_2^{(2)})$, highlighted in Fig. 10(a3), Node 1 enters the postictal state ($z_1^{(1)}$ falling) while Node 2 remains in the ictal state ($z_1^{(2)}$ rising). The coupling term in Eq. (12), which acts to align the two nodes' discharge states, accelerates the decay of $z_1^{(1)}$ and thereby drives $p^{(1)}$ rapidly toward $\mathrm{TH}_{\mathrm{spike}}$, compressing Node 1's postictal recovery window. Once Node 2 enters its postictal period at $T_2^{(2)}$, both $z_1^{(1)}$ and $z_1^{(2)}$ decay simultaneously. The coupling-mediated driving force then diminishes,

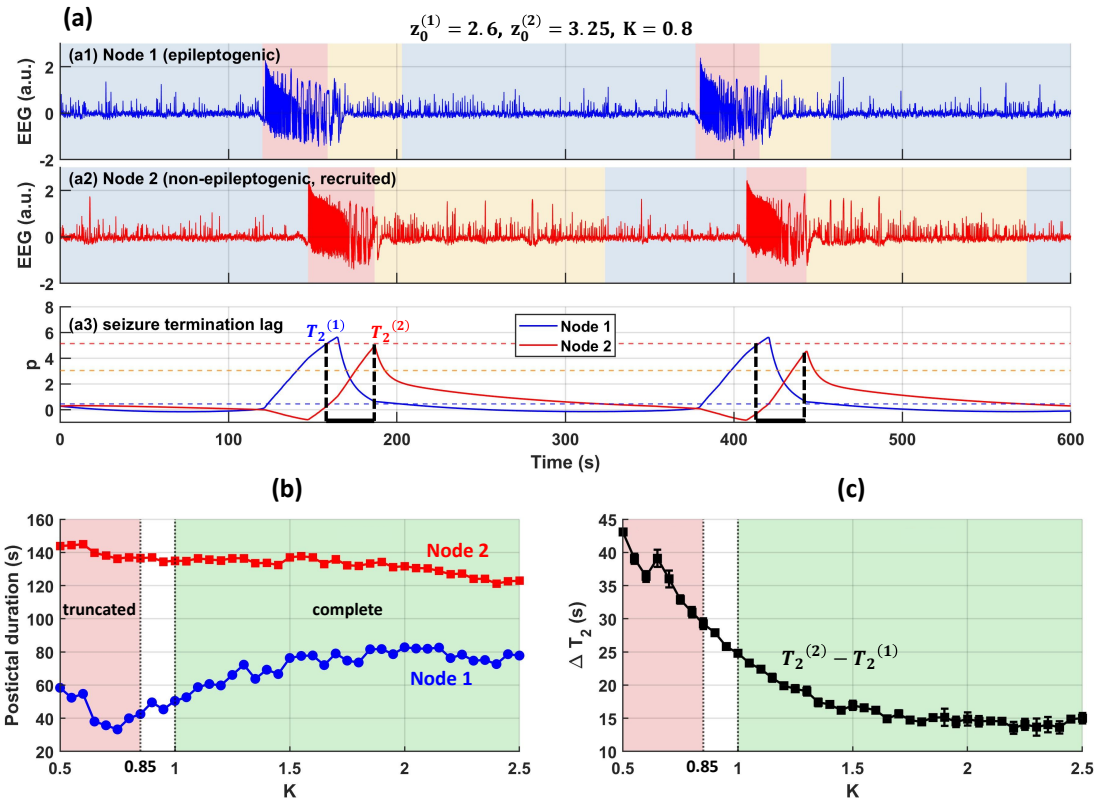


Fig. 10 Postictal-duration differences and termination lags in two coupled model nodes. **(a)** Simulations at coupling strength $K = 0.8$, with epileptogenicity parameters $z_0^{(1)} = 2.6$ and $z_0^{(2)} = 3.25$. Panels (a1,a2) show the simulated EEG for the driving Node 1 (blue) and recruited Node 2 (red); panel (a3) shows their effective drives p. Blue, pink, and yellow shading denotes model-defined interictal, ictal, and postictal periods. Horizontal dashed lines mark the spike (blue, 0.43), spike–wave discharge (orange, 3.03), and wave (red, 5.12) thresholds. The highlighted interval $(T_2^{(1)}, T_2^{(2)})$ marks the lag between termination times $T_2^{(1)}$ and $T_2^{(2)}$ of the two nodes. For complete transitions, T_2 is the upward wave-threshold crossing; for truncated transitions, including Node 2 here, it is the onset of p decline. **(b)** Mean postictal duration, $T_3 - T_2$, versus K for Node 1 (blue circles) and Node 2 (red squares). The recovery endpoint T_3 is the subsequent downward spike-threshold crossing. **(c)** Mean termination lag, $\Delta T_2 = T_2^{(2)} - T_2^{(1)}$, versus K. Black squares and error bars denote the mean and standard deviation across detected event pairs, respectively. In (b,c), pink and green shading marks truncated and complete transitions in Node 2, respectively; the unshaded interval $0.85 \leq K < 1$ contains both.

and Node 2's postictal recovery proceeds largely unperturbed. Under inter-node coupling, postictal duration is therefore not solely determined by the $p_{\max}$ attained during the seizure, but is additionally modulated by the seizure termination lag $\Delta T_2 = T_2^{(2)} - T_2^{(1)}$ between nodes, which selectively compresses the driving node's postictal interval. Furthermore, this lag is an intrinsic feature of the recruitment dynamics and persists at all coupling strengths. As shown in Fig. 10(c), ΔT_2 decreases monotonically with increasing K but converges to an asymptotic value near 15 s rather than vanishing entirely. Consequently, the postictal duration difference in Fig. 10(b) narrows with stronger coupling but remains substantial, reflecting the irreducible temporal lag inherent to the recruitment dynamics.

Taken together, the two-node analysis reveals two coupling-dependent differences between spontaneous and recruited seizure-like events. First, coupling strength determines how far recruited rhythm transitions progress toward slow-wave activity: weak coupling produces truncated transitions lacking slow-wave components, whereas stronger coupling yields transitions that reach the wave regime and become comparable to those of the driving node. Second, recruited events exhibit longer model-defined postictal durations than spontaneous events in the driving node because

of a persistent termination lag between the two nodes. These model-derived spectral and temporal differences may serve as candidate dynamical signatures for distinguishing driving from passively recruited nodes in epileptic networks, subject to clinical validation.

4 Discussion

Epileptic EEG reflects biophysical processes operating over widely separated timescales, giving rise to rich rhythmic and spectral dynamics. Previous studies have documented the slowing of rhythmic discharges during seizure evolution and prominent delta activity after seizure termination (Perucca et al. 2014; Demont-Guignard et al. 2009; Pottkamper et al. 2020; So and Blume 2010). Quantitative studies have also characterized ictal harmonic structures (Hu et al. 2026) and linked postictal reductions in spectral entropy to increased relative delta power (Sanz-García et al. 2017). These observations motivate investigating how fast ictal activity and slower recovery-related processes interact to generate the fast-to-slow rhythm transition. To this end, we developed the multi-timescale DCE model, which couples fast ictal activity with SWD-related dynamics while preserving spontaneous interictal–ictal switching. The simulated EEG qualitatively captures progressive ictal rhythm slowing and the persistence of slow activity into a model-defined postictal phase. The model thus provides a unified dynamical account of this spectral evolution within recurrent seizure cycles.

The within-patient analysis illustrates ictal rhythm slowing followed by retained relative low-frequency weighting during early postictal recovery (Fig. 3). The extended cohort analysis reveals variability in postictal spectral trajectories across patients (Supplementary Table S4). These observations motivate viewing ictal slowing and subsequent low-frequency activity as successive components of a continuous spectral trajectory spanning the ictal and early postictal periods. Previous studies likewise indicate that electrophysiological recovery can extend beyond seizure termination (Fisher and Schachter 2000; Pottkamper et al. 2020; Bratu et al. 2024). The continuation of spectral evolution beyond seizure offset is compatible with a transition into a dynamically distinct postictal state (Kramer et al. 2012; Bauer et al. 2017). Changes in discharge morphology, background activity, spectral entropy, and synchronization provide complementary information about seizure termination (Pottkamper et al. 2020; Sanz-García et al. 2017; Kramer et al. 2012). Postictal slow activity can also be accompanied by residual spikes (Pottkamper et al. 2020). Within the DCE model, the continuously evolving effective drive p organizes waveform evolution, with oscillatory-regime thresholds used to distinguish model phases. During subsequent postictal recovery, the effective drive p declines through the SWD and spike regimes, permitting transient postictal spikes before falling below the spike threshold. These model-generated spikes provide a qualitative counterpart to residual postictal activity (Supplementary Section S3.1 and Fig. S3(d3)). Their relationship to flickering between ictal and postictal states near seizure termination remains to be established (Kramer et al. 2012). The model thus links ictal slowing, postictal slow activity, and transient recovery spikes while retaining a distinct, model-defined ictal–postictal boundary.

Within the DCE framework, the fast-to-slow rhythm transition emerges from reciprocal nonlinear coupling between the two subsystems rather than from a simple superposition of independent fast and slow oscillations. On the one hand, the activity of Subsystem I, represented by x_1, is low-pass filtered and combined with the ultraslow variable z_1 to form the effective drive p for Subsystem II. As p increases during a seizure-like event, it drives Subsystem II successively through the spike, SWD, and wave regimes, thereby increasing the dominant oscillatory timescale and shifting spectral power toward lower frequencies. On the other hand, the activity of Subsystem II, represented by x_2, reshapes the x_1-nullcline and thereby modulates the amplitude envelope of fast ictal activity in Subsystem I. The simulated rhythm transition therefore arises from coordinated changes in waveform, oscillatory regime, and amplitude envelope. This reciprocal organization is consistent with clinical observations that fast ictal discharges and spike–wave complexes can overlap and evolve continuously (Aung et al. 2026). Although the DCE model is phenomenological, its architecture draws on physiologically motivated descriptions of epileptic activity. Subsystem I represents an

effective fast-discharge component, whereas Subsystem II follows a reduced thalamocortical architecture in which fast excitation and inhibition interact with slower inhibitory feedback to generate SWDs (Destexhe 1998; Steriade and Contreras 1998; Wang et al. 2012). In particular, $GABA_B$-mediated inhibition provides a physiological motivation for the slow feedback represented by z_2 (Destexhe 1998; Otis and Mody 1992). However, z_2 is an effective dynamical variable rather than a quantitative representation of a receptor-specific current. In the DCE model, rhythm slowing arises from evolving state variables and p-driven regime transitions under fixed connectivity and timescale parameters. These results explain how interacting fast and slow components can organize spectral evolution; linking this evolution to changes in specific neurotransmitter systems requires independent physiological validation. Other processes, including ionic and metabolic regulation, adenosine-mediated suppression, and postictal hypoperfusion or hypoxia, may also contribute to seizure termination and recovery but are not explicitly represented in the model (Frohlich et al. 2010; Pottkamper et al. 2020; Liou et al. 2020; Farrell et al. 2016).

The parameter analysis in Section 3.3 revealed how heterogeneous fast-to-slow rhythm transitions can emerge from a common dynamical architecture. Specifically, three functionally distinct parameter families control different aspects of the transition: timescale ratios determine its spectral span, the filtering rates γ_1 and γ_2 govern its temporal organization, and the connectivity coefficients C_{zx} and C_{xz} shape the availability and relative occupancy of the spike, SWD, and wave regimes. This parameter-to-phenotype mapping extends the node-level representation of the DCE model beyond a single epileptogenicity parameter, allowing nodes with similar seizure propensities to exhibit distinct rhythm-transition phenotypes. This flexibility could support richer node-level parameterization when fitting heterogeneous EEG phenotypes across brain regions or patients and suggests a potential application in patient-specific estimation of electrographic seizure offset. Specifically, DCE parameters could first be identified from clinician-annotated training seizures by fitting their spectrotemporal trajectories and aligning the model-defined ictal–postictal boundary with the annotated offsets. For subsequent seizures, the fitted model could be used to reconstruct the latent trajectory $p(t)$, whose upward crossing of the wave-regime threshold derived from the fitted bifurcation structure would provide a model-based estimate of seizure offset. Realizing this application will require formal identifiability and uncertainty analyses, reliable state estimation, and validation against expert annotations in held-out seizures (Raue et al. 2009; Villaverde et al. 2022; Hashemi et al. 2020). Assigning physiological meaning to the fitted parameters would additionally require validation against independent physiological measurements (Vattikonda et al. 2021).

The two-node analysis in Section 3.4 extends the DCE framework from isolated-node dynamics to a minimal setting of inter-node seizure recruitment. The recruitment-mode map in Fig. 8(a) shows that local epileptogenicity and inter-node coupling jointly determine whether the two nodes exhibit one-to-one entrainment, many-to-one recruitment, recruitment failure, or suppression. For the intrinsically non-epileptogenic node, this map indicates that it can remain silent, respond only after repeated driving events, or become entrained depending on coupling strength. Within the recruitment regime, coupling strength further governs how far recruited rhythm transitions progress through the spike, SWD, and wave regimes, a property quantified here as rhythm transition completeness. As shown in Fig. 9(a,b), at weak coupling, the p trajectories of recruited events reach only the SWD regime, producing truncated transitions without a slow-wave component. As coupling increases, an increasing proportion of recruited events cross the wave-regime threshold, eventually producing complete transitions resembling those of the driving node. Coupling therefore shapes not only whether recruitment occurs, but also the internal oscillatory composition of recruited seizure-like events. These behaviors are consistent with the broader view that seizure propagation and termination emerge from interactions between local dynamics and network connectivity (Proix et al. 2018; Vattikonda et al. 2021; Proix et al. 2017). It should be noted that the coupling implemented here is an effective symmetric interaction acting through the dynamics of the ultraslow variable z_1 in each node, rather than a reconstruction of directed axonal pathways or conduction delays.

From the perspective of epileptic network analysis, the simulations in Sections 3.4.2 and 3.4.3 suggest that rhythm transition completeness and postictal duration may provide complementary information about node roles. Rhythm transition completeness captures a spectral dimension of recruitment, describing how far an event progresses toward slow-wave activity. Weak coupling produces truncated transitions in which the recruited node does not enter all oscillatory regimes expressed by the driving node, whereas stronger coupling progressively reduces this spectral difference. It may therefore reflect recruitment strength, but cannot serve as a coupling-independent marker for distinguishing driving from recruited nodes. Postictal duration provides a second, temporal dimension. In the tested two-node configurations, the model predicts longer postictal durations in recruited events than in spontaneous events in the driving node. Clinical intracranial studies have associated distributed seizure propagation with stronger postictal delta activity and altered global connectivity (Tomlinson et al. 2018), while SEEG studies indicate that electrophysiological recovery can substantially outlast the seizure itself (Bratu et al. 2024). These findings motivate investigating regional differences in postictal recovery, although they do not directly establish the predicted duration difference between driving and recruited regions. Together with the model results, they raise the possibility that recruited regions contribute to postictal dysfunction even when seizure initiation is driven elsewhere. Rhythm transition completeness and postictal duration may consequently serve as candidate dynamical signatures for distinguishing actively driving from passively recruited nodes, subject to clinical validation. This model-level distinction may relate to, but should not be equated directly with, the clinical distinction between epileptogenic and propagation zones. Relating these electrophysiological features to postictal symptoms additionally requires consideration of behavioral, vascular, and metabolic processes beyond the current model, including hypoperfusion and hypoxia (Farrell et al. 2016). Validation will require SEEG or other spatially resolved recordings with independently identified seizure-onset and recruited regions, using a common recovery criterion across regions.

Methodologically, a central contribution of this study is to treat the EEG time–frequency representation as a dynamical phenotype to be generated and explained, rather than solely as a feature space for seizure detection or classification. In many studies of seizure detection and prediction, time–frequency measures are commonly extracted as descriptive features or used as inputs to machine-learning models, including deep neural networks (Alotaiby et al. 2014; Xu et al. 2024; Zhang et al. 2024). Existing generative models, by contrast, have addressed distinct aspects of epileptic dynamics. NMMs have reproduced specific epileptiform patterns, including fast ictal activity and SWDs, and have related these patterns to changes in excitation, inhibition, and population coupling (Wendling et al. 2002; Goodfellow et al. 2011; Taylor and Baier 2011). The Epileptor model provides a low-dimensional description of spontaneous seizure onset and offset and has enabled patient-specific modeling of seizure propagation through whole-brain networks (Jirsa et al. 2014; Proix et al. 2017). Other models have described within-seizure waveform evolution, progressive ictal slowing, seizure termination, or postictal suppression through trajectories in parameter space, critical transitions, adaptive inhibition, or network plasticity (Nevado-Holgado et al. 2012; Kramer et al. 2012; Bauer et al. 2017; Liou et al. 2020). In particular, Kayabas et al. (2024) modeled the decreasing frequency of fast-onset activity using a physiologically motivated NMM. That gamma-band chirp is distinct from the longer ictal-to-postictal spectral redistribution emphasized here. The DCE fast component can show a local increase in frequency at seizure onset and does not reproduce that specific downward chirp. Its overall spectral slowing reflects changes in waveform composition and relative component amplitudes. The DCE model should therefore be viewed as complementary to these approaches. Its specific contribution is to combine recurrent interictal–ictal switching, a progressive spike-to-SWD-to-wave cascade, and an explicit postictal recovery interval within a unified dynamical framework. In this way, the DCE model links observable EEG time–frequency patterns to transitions among its dynamical regimes. Its ability to autonomously generate recurrent interictal–ictal–postictal cycles may facilitate future fitting to long-term EEG recordings.

This study has several limitations. First, the clinical analysis was limited to a single scalp EEG dataset and early postictal recovery. The observed between-patient variability highlights the need for independent scalp and intracranial EEG studies to assess the prevalence and generalizability of this spectrotemporal pattern. Second, the DCE variables are phenomenological rather than quantitative measurements of specific neuronal or synaptic processes. Although this abstraction limits direct physiological interpretation, the compact model structure facilitates explicit dynamical analysis of rhythm interactions across timescales. Finally, the two-node system represents only a minimal network extension and does not incorporate directed anatomical connectivity. Future work will construct patient-specific large-scale whole-brain models based on DCE nodes, parameterize inter-node coupling using individual structural connectomes, and estimate node-level model parameters by matching simulated spectral phenotypes to multichannel EEG recordings (Proix et al. 2018; Vattikonda et al. 2021; Proix et al. 2017). Such extensions will enable direct testing of whether transition completeness and postictal duration provide additional information for distinguishing actively driving from passively recruited regions.

5 Conclusion

Clinical EEG analysis provided an empirical reference for the fast-to-slow rhythm transition, linking ictal slowing with retained relative low-frequency weighting during early postictal recovery. The expression of this spectral pattern varied across seizures and patients. The proposed Dual-Component Epileptic EEG (DCE) model qualitatively reproduced the principal spectral features of this pattern within recurrent interictal–ictal–postictal cycles. Mechanistically, the transition emerged from nonlinear coupling between fast ictal activity and SWD-related dynamics, with the effective drive p organizing a cascade through the spike, SWD, and wave regimes. Parameter analyses further decomposed rhythm-transition variability into three dimensions: spectral span, temporal organization, and oscillatory-regime composition. In the two-node simulations, coupling controlled the extent of rhythm slowing in recruited events, which exhibited longer model-defined postictal durations than spontaneous events in the driving node. These spectral and temporal differences suggest candidate dynamical signatures for distinguishing actively driving from passively recruited regions, pending validation in spatially resolved clinical recordings. Together, these findings provide a unified dynamical framework for investigating the generation, variability, and network modulation of ictal-to-postictal spectral evolution. The autonomous recurrence and node-level rhythmic flexibility of the DCE model may support future fitting to long-duration EEG recordings and extensions to patient-specific whole-brain models.

Supplementary information. The supplementary material provides the stochastic formulation and numerical implementation of the DCE model (Section S1), extended clinical EEG methods and analyses (Section S2), component-level simulations and controlled coupling analyses (Section S3), and a qualitative comparison with the original Epileptor model (Section S4).

Statements and Declarations

Funding. This work was supported by the National Natural Science Foundation of China under Grant Nos. 62571367, 62271348, and 62171312.

Competing Interests. The authors have no relevant financial or non-financial interests to disclose.

Ethics approval. This study involved secondary analysis of publicly available, de-identified EEG recordings from the Siena Scalp EEG Database. No participants were recruited and no new human data were collected. According to the database documentation, the original data collection was approved by the Ethical Committee of the University of Siena in accordance with the Declaration of Helsinki.

Consent to participate. According to the Siena Scalp EEG Database documentation, written informed consent for recording and scientific use of the data was obtained from the participants during the original data collection.

Consent for publication. Not applicable. This article does not contain identifiable personal information.

Data availability. The EEG data analyzed in Section 3.1 are publicly available from the Siena Scalp EEG Database hosted by PhysioNet at https://physionet.org/content/siena-scalp-eeg/1.0.0/. The simulated data were generated using the DCE model and parameter settings described in the manuscript.

Code availability. The MATLAB implementation of the DCE model described in Section S1 is available at https://github.com/Fengzhang1998/Dual-Component-Epileptic-EEG-model.

Author contributions. All authors contributed to the study conception and design. Model implementation, numerical simulation, and analysis were performed by Feng Zhang. The first draft of the manuscript was written by Feng Zhang and all authors commented on previous versions of the manuscript. All authors read and approved the final manuscript.

References

Alotaiby TN, Alshebeili SA, Alshawi T, et al (2014) EEG seizure detection and prediction algorithms: a survey. EURASIP Journal on Advances in Signal Processing 2014(1):183. https://doi.org/10.1186/1687-6180-2014-183

Aung T, Jegou A, Chauvel P (2026) Spike-fast activity interplay: A gateway to seizure. Epilepsia 67(2):878–894. https://doi.org/10.1111/epi.18703

Bartolomei F, Wendling F, Régis J, et al (2004) Pre-ictal synchronicity in limbic networks of mesial temporal lobe epilepsy. Epilepsy Research 61(1-3):89–104. https://doi.org/10.1016/j.eplepsyres.2004.06.006

Bartolomei F, Chauvel P, Wendling F (2008) Epileptogenicity of brain structures in human temporal lobe epilepsy: a quantified study from intracerebral EEG. Brain 131(7):1818–1830. https://doi.org/10.1093/brain/awn111

Bauer PR, Thijs RD, Lamberts RJ, et al (2017) Dynamics of convulsive seizure termination and postictal generalized EEG suppression. Brain 140(3):655–668. https://doi.org/10.1093/brain/aww322

Bratu IF, Medina Villalon S, Garnier E, et al (2024) How fast does the brain recover after an epileptic seizure? Annals of Clinical and Translational Neurology 11(6):1630–1635. https://doi.org/10.1002/acn3.52073

Comsa IM, Bekinschtein TA, Chennu S (2019) Transient topographical dynamics of the electroencephalogram predict brain connectivity and behavioural responsiveness during drowsiness. Brain Topography 32:315–331. https://doi.org/10.1007/s10548-018-0689-9

De Curtis M, Librizzi L, Biella G (2001) Discharge threshold is enhanced for several seconds after a single interictal spike in a model of focal epileptogenesis. European Journal of Neuroscience 14(1):174–178. https://doi.org/10.1046/j.0953-816x.2001.01637.x

Demont-Guignard S, Benquet P, Gerber U, et al (2009) Analysis of intracerebral EEG recordings of epileptic spikes: insights from a neural network model. IEEE Transactions on Biomedical Engineering 56(12):2782–2795. https://doi.org/10.1109/tbme.2009.2028015

Destexhe A (1998) Spike-and-wave oscillations based on the properties of GABAB receptors. The Journal of Neuroscience 18(21):9099–9111. https://doi.org/10.1523/jneurosci.18-21-09099.1998

Detti P (2020) Siena Scalp EEG Database. PhysioNet, https://doi.org/10.13026/5d4a-j060, version 1.0.0

Ermentrout GB, Terman DH (2010) Bursting oscillations. In: Mathematical Foundations of Neuroscience, Interdisciplinary Applied Mathematics, vol 35. Springer, New York, NY, p 103–127, https://doi.org/10.1007/978-0-387-87708-2_5

Farrell JS, Gaxiola-Valdez I, Wolff MD, et al (2016) Postictal behavioural impairments are due to a severe prolonged hypoperfusion/hypoxia event that

is COX-2 dependent. eLife 5:e19352. https://doi.org/10.7554/elife.19352

Fisher RS, Schachter SC (2000) The postictal state: A neglected entity in the management of epilepsy. Epilepsy & Behavior 1(1):52–59. https://doi.org/10.1006/ebeh.2000.0023

Frauscher B, Bartolomei F, Kobayashi K, et al (2017) High-frequency oscillations: The state of clinical research. Epilepsia 58(8):1316–1329. https://doi.org/10.1111/epi.13829

Frohlich F, Sejnowski TJ, Bazhenov M (2010) Network bistability mediates spontaneous transitions between normal and pathological brain states. The Journal of Neuroscience 30(32):10734–10743. https://doi.org/10.1523/jneurosci.1239-10.2010

Goodfellow M, Schindler K, Baier G (2011) Intermittent spike-wave dynamics in a heterogeneous, spatially extended neural mass model. NeuroImage 55(3):920–932. https://doi.org/10.1016/j.neuroimage.2010.12.074

Hashemi M, Vattikonda AN, Sip V, et al (2020) The Bayesian virtual epileptic patient: A probabilistic framework designed to infer the spatial map of epileptogenicity in a personalized large-scale brain model of epilepsy spread. NeuroImage 217:116839. https://doi.org/10.1016/j.neuroimage.2020.116839

Hu L, Ye L, Ye H, et al (2026) Harmonic patterns embedded in ictal EEG signals in focal epilepsy: new insight into the epileptogenic zone. BMC Medicine 24(1):115. https://doi.org/10.1186/s12916-026-04665-7

Jirsa VK, Stacey WC, Quilichini PP, et al (2014) On the nature of seizure dynamics. Brain 137(8):2210–2230. https://doi.org/10.1093/brain/awu133

Kane N, Acharya J, Beniczky S, et al (2017) A revised glossary of terms most commonly used by clinical electroencephalographers and updated proposal for the report format of the EEG findings. revision 2017. Clinical Neurophysiology Practice 2:170–185. https://doi.org/10.1016/j.cnp.2017.07.002

Kayabas MA, Köksal Ersöz E, Yochum M, et al (2024) Transition to seizure in focal epilepsy: From SEEG phenomenology to underlying mechanisms. Epilepsia 65(12):3619–3630. https://doi.org/10.1111/epi.18173

Kramer MA, Truccolo W, Eden UT, et al (2012) Human seizures self-terminate across spatial scales via a critical transition. Proceedings of the National Academy of Sciences 109(51):21116–21121. https://doi.org/10.1073/pnas.1210047110

Lee S, Issa NP, Rose S, et al (2020) DC shifts, high frequency oscillations, ripples and fast ripples in relation to the seizure onset zone. Seizure 77:52–58. https://doi.org/10.1016/j.seizure.2019.05.001

Liou Jy, Smith EH, Bateman LM, et al (2020) A model for focal seizure onset, propagation, evolution, and progression. eLife 9:e50927. https://doi.org/10.7554/elife.50927

Nevado-Holgado AJ, Marten F, Richardson MP, et al (2012) Characterising the dynamics of EEG waveforms as the path through parameter space of a neural mass model: Application to epilepsy seizure evolution. NeuroImage 59(3):2374–2392. https://doi.org/10.1016/j.neuroimage.2011.08.111

Otis TS, Mody I (1992) Differential activation of GABAA and GABAB receptors by spontaneously released transmitter. Journal of Neurophysiology 67(1):227–235. https://doi.org/10.1152/jn.1992.67.1.227

Perucca P, Dubeau F, Gotman J (2014) Intracranial electroencephalographic seizure-onset patterns: effect of underlying pathology. Brain 137(1):183–196. https://doi.org/10.1093/brain/awt299

Pottkamper JCM, Hofmeijer J, van Waarde JA, et al (2020) The postictal state - what do we know? Epilepsia 61(6):1045–1061. https://doi.org/10.1111/epi.16519

Proix T, Bartolomei F, Guye M, et al (2017) Individual brain structure and modelling predict seizure propagation. Brain 140(3):641–654.

https://doi.org/10.1093/brain/awx004

Proix T, Jirsa VK, Bartolomei F, et al (2018) Predicting the spatiotemporal diversity of seizure propagation and termination in human focal epilepsy. Nature Communications 9(1):1088. https://doi.org/10.1038/s41467-018-02973-y

Raue A, Kreutz C, Maiwald T, et al (2009) Structural and practical identifiability analysis of partially observed dynamical models by exploiting the profile likelihood. Bioinformatics 25(15):1923–1929. https://doi.org/10.1093/bioinformatics/btp358

Rosenow F, Lüders H (2001) Presurgical evaluation of epilepsy. Brain 124(9):1683–1700. https://doi.org/10.1093/brain/124.9.1683

Saggio ML, Crisp D, Scott JM, et al (2020) A taxonomy of seizure dynamotypes. eLife 9:e55632. https://doi.org/10.7554/elife.55632

Sanz-García A, Vega-Zelaya L, Pastor J, et al (2017) Towards operational definition of postictal stage: Spectral entropy as a marker of seizure ending. Entropy 19(2):81. https://doi.org/10.3390/e19020081

Sheybani L, De Stefano P, Seeck M, et al (2025) EEG focal delta slowing in focal epilepsy – a didactic review. Clinical Neurophysiology Practice 10:392–401. https://doi.org/10.1016/j.cnp.2025.09.001

Sitnikova E (2010) Thalamo-cortical mechanisms of sleep spindles and spike–wave discharges in rat model of absence epilepsy (a review). Epilepsy Research 89(1):17–26. https://doi.org/10.1016/j.eplepsyres.2009.09.005

So NK, Blume WT (2010) The postictal EEG. Epilepsy & Behavior 19(2):121–126. https://doi.org/10.1016/j.yebeh.2010.06.033

Steriade M, Contreras D (1998) Spike-wave complexes and fast components of cortically generated seizures. i. role of neocortex and thalamus. Journal of Neurophysiology 80(3):1439–1455. https://doi.org/10.1152/jn.1998.80.3.1439

Taylor PN, Baier G (2011) A spatially extended model for macroscopic spike-wave discharges. Journal of Computational Neuroscience 31(3):679–684. https://doi.org/10.1007/s10827-011-0332-1

Tomlinson SB, Khambhati AN, Bermudez C, et al (2018) Alterations of network synchrony after epileptic seizures: An analysis of post-ictal intracranial recordings in pediatric epilepsy patients. Epilepsy Research 143:41–49. https://doi.org/10.1016/j.eplepsyres.2018.04.003

Vattikonda AN, Hashemi M, Sip V, et al (2021) Identifying spatio-temporal seizure propagation patterns in epilepsy using Bayesian inference. Communications Biology 4(1):1244. https://doi.org/10.1038/s42003-021-02751-5

Villaverde AF, Pathirana D, Fröhlich F, et al (2022) A protocol for dynamic model calibration. Briefings in Bioinformatics 23(1):bbab387. https://doi.org/10.1093/bib/bbab387

Wang Y, Goodfellow M, Taylor PN, et al (2012) Phase space approach for modeling of epileptic dynamics. Physical Review E 85(6):061918. https://doi.org/10.1103/physreve.85.061918

Wendling F, Bartolomei F, Bellanger JJ, et al (2002) Epileptic fast activity can be explained by a model of impaired GABAergic dendritic inhibition. European Journal of Neuroscience 15(9):1499–1508. https://doi.org/10.1046/j.1460-9568.2002.01985.x

Wendling F, Bartolomei F, Bellanger JJ, et al (2003) Epileptic fast intracerebral EEG activity: evidence for spatial decorrelation at seizure onset. Brain 126(6):1449–1459. https://doi.org/10.1093/brain/awg144

Wendling F, Benquet P, Bartolomei F, et al (2016) Computational models of epileptiform activity. Journal of Neuroscience Methods 260:233–251. https://doi.org/10.1016/j.jneumeth.2015.03.027

Wilcox RR, Rousselet GA (2023) An updated guide to robust statistical methods in neuroscience. Current Protocols 3(3):e719. https://doi.org/10.1002/cpz1.719

Wilson HR, Cowan JD (1972) Excitatory and inhibitory interactions in localized populations of model neurons. Biophysical Journal 12(1):1–24. https://doi.org/10.1016/s0006-3495(72)86068-5

Wong S, Simmons A, Rivera-Villicana J, et al (2023) EEG datasets for seizure detection and prediction— a review. Epilepsia Open 8(2):252–267. https://doi.org/10.1002/epi4.12704

Xu J, Yan K, Deng Z, et al (2024) EEG-based epileptic seizure detection using deep learning techniques: A survey. Neurocomputing 610:128644. https://doi.org/10.1016/j.neucom.2024.128644

Zhang F, Wei X, Lu L (2024) A multi-frame network model based on time-frequency analysis for epilepsy prediction. In: 2024 43rd Chinese Control Conference (CCC). IEEE, pp 8262–8267, https://doi.org/10.23919/ccc63176.2024.10662334

Zijlmans M, Jiruska P, Zelmann R, et al (2012) High-frequency oscillations as a new biomarker in epilepsy. Annals of Neurology 71(2):169–178. https://doi.org/10.1002/ana.22548

Supplementary Files

This is a list of supplementary files associated with this preprint. Click to download.

- ESM1.pdf